No detergents were used, as they can reduce the degree of glutamic acid decarboxylase (GAD) immunostaining. Slices were then incubated overnight in PBS containing 1% bovine serum albumin and 0.05% sodium azide, before being incubated in mixture of rabbit polyclonal anti-glycine antibody (1:10,000; Chemicon) and goat polyclonal S3 antibody against GAD (1:2,000; NIMH Laboratory of Clinical Science) for 5 d at 20 °C. The S3 antibody recognizes both GAD65 and GAD67 forms[40]. After this, the sections were rinsed briefly in PBS, and then incubated with a mixture of fluorescein isothiocyanate (FITC)-conjugated donkey anti-rabbit antibody (1:1,000; Jackson Immunoresearch) and rhodamine red-conjugated donkey anti-goat antibody (1:1,000; Jackson Immunoresearch) for 3 h. The sections were rinsed briefly in PB, mounted in Vectashield (Vector Laboratories) and examined with a confocal laser-scanning microscope (CLSM; TCS-SP2; Leica). Single laser beams, of 488 and 543 nm in wavelength, were alternately focused on to the specimen to collect fluorescent images for FITC (glycine) and rhodamine red (GAD), respectively. In the absence of the primary antibodies, only negligible background staining was observed in the LSO (data not shown), confirming the specificity of our GAD and glycine immunolabeling.

Note: Supplementary information is available on the Nature Neuroscience website.

ACKNOWLEDGMENTS

We thank A. Moorhouse for discussion and editing of the manuscript, and N. Akaike for technical advice. We also thank O.P. Otterson, I.J. Kopin, W.H. Oertel, D.E. Schmechel and M.L. Tappaz for help obtaining antibodies. This work was supported by research grants from the Ministry of Education, Culture, Sports, Science and Technology, Japan (15016082, 15650076 and 15390065 to J.N).

COMPETING INTERESTS STATEMENT

The authors declare that they have no competing financial interests.

Received 4 July; accepted 1 December 2003
Published online at http://www.nature.com/natureneuroscience/

1. Ornung, G. *et al.* Qualitative and quantitative analysis of glycine- and GABA-immunoreactive nerve terminals on motoneuron cell bodies in the cat spinal cord: a postembedding electron microscopic study. *J. Comp. Neurol.* **365**, 413–426 (1996).
2. Yang, H.W., Min, M.Y., Appenteng, K. & Batten, T.F. Glycine-immunoreactive terminals in the rat trigeminal motor nucleus: light- and electron-microscopic analysis of their relationships with motoneurones and with GABA-immunoreactive terminals. *Brain Res.* **749**, 301–319 (1997).
3. Levi, S., Chesnoy-Marchais, D., Sieghart, W. & Triller, A. Synaptic control of glycine and $GABA_A$ receptors and gephyrin expression in cultured motoneurons. *J. Neurosci.* **19**, 7434–7449 (1999).
4. Kneussel, M. & Betz, H. Receptors, gephyrin and gephyrin-associated proteins: novel insights into the assembly of inhibitory postsynaptic membrane specializations. *J. Physiol.* **525**, 1–9 (2000).
5. O'Brien, J.A. & Berger, A.J. Cotransmission of GABA and glycine to brain stem motoneurons. *J. Neurophysiol.* **82**, 1638–1641 (1999).
6. Jonas, P., Bischofberger, J. & Sandkuhler, J. Co-release of two fast neurotransmitters at a central synapse. *Science* **281**, 419–424 (1998).
7. Russier, M., Kopysova, I.L., Ankri, N., Ferrand, N. & Debanne, D. GABA and glycine co-release optimizes functional inhibition in rat brainstem motoneurons *in vitro*. *J. Physiol.* **541**,123–137 (2002).
8. Kotak, V.C., Korada, S., Schwartz, I.R. & Sanes, D.H. A developmental shift from GABAergic to glycinergic transmission in the central auditory system. *J. Neurosci.* **18**, 4646–4655 (1998).
9. Smith, A.J., Owens, S. & Forsythe, I.D. Characterization of inhibitory and excitatory postsynaptic currents of the rat medial superior olive. *J. Physiol.* **529**, 681–698 (2000).
10. Sanes, D.H. & Friauf, E. Development and influence of inhibition in the lateral superior olivary nucleus. *Hear. Res.* **147**, 46–58 (2000).
11. Korada, S. & Schwartz, I.R. Development of GABA, glycine, and their receptors in the auditory brainstem of gerbil: a light and electron microscopic study. *J. Comp. Neurol.* **409**, 664–681 (1999).
12. del Castillo, J. & Katz, B. Quantal components of end-plate potential. *J. Physiol.* **124**, 560–573 (1954).
13. Walmsley, B., Alvarez, F.J. & Fyffe, R.E. Diversity of structure and function at mammalian central synapses. *Trends Neurosci.* **21**, 81–88 (1998).
14. Akaike, N. & Moorhouse, A.J. Techniques: applications of the nerve-bouton preparation in neuropharmacology. *Trends Pharmacol. Sci.* **24**, 44–47 (2003).
15. Dumoulin, A., Triller, A. & Dieudonne, S. IPSC kinetics at identified GABAergic and mixed GABAergic and glycinergic synapses onto cerebellar Golgi cells. *J. Neurosci.* **21**, 6045–6057 (2001).
16. Keller, A.F., Coull, J.A., Chery, N., Poisbeau, P. & De Koninck, Y. Region-specific developmental specialization of GABA-glycine cosynapses in laminas I-II of the rat spinal dorsal horn. *J. Neurosci.* **21**, 7871–7880 (2001).
17. Friauf, E, Hammerschmidt, B. & Kirsch, J. Development of adult-type inhibitory glycine receptors in the central auditory system of rats. *J. Comp. Neurol.* **385**, 117–134 (1997).
18. Otis, T.S., De Koninck, Y. & Mody, I. Lasting potentiation of inhibition is associated with an increased number of gamma-aminobutyric acid type A receptors activated during miniature inhibitory postsynaptic currents. *Proc. Natl. Acad. Sci. USA* **91**, 7698–7702 (1994).
19. Sanes, D.H. & Siverls, V. Development and specificity of inhibitory terminal arborizations in the central nervous system. *J. Neurobiol.* **22**, 837–854 (1991).
20. Kim, G. & Kandler, K. Elimination and strengthening of glycinergic/GABAergic connections during tonotopic map formation. *Nat. Neurosci.* **6**, 282–290 (2003).
21. Gasnier, B. The loading of neurotransmitters into synaptic vesicles. *Biochimie* **82**, 327–337 (2000).
22. Schotzinger, R.J. & Landis, S.C. Cholinergic phenotype developed by noradrenergic sympathetic neurons after innervation of a novel cholinergic target *in vivo*. *Nature* **335**, 637–639 (1988).
23. Habecker, B.A., Tresser, S.J., Rao, M.S. & Landis, S.C. Production of sweat gland cholinergic differentiation factor depends on innervation. *Dev. Biol.* **167**, 307–316 (1995).
24. Rietzel, H.J. & Friauf, E. Neuron types in the rat lateral superior olive and developmental changes in the complexity of their dendritic arbors. *J. Comp. Neurol.* **390**, 20–40 (1998).
25. Takahashi, T., Momiyama, A., Hirai, K., Hishinuma, F. & Akagi, H. Functional correlation of fetal and adult forms of glycine receptors with developmental changes in inhibitory synaptic receptor channels. *Neuron* **9**, 1155–1161 (1992).
26. Kakazu, Y., Akaike, N., Komiyama, S. & Nabekura, J. Regulation of intracellular chloride by cotransporters in developing lateral superior olive neurons. *J. Neurosci.* **19**, 2843–2851 (1999).
27. Kandler, K. & Friauf E. Development of glycinergic and glutamatergic synaptic transmission in the auditory brainstem of perinatal rats. *J. Neurosci.* **15**, 6890–6904 (1995).
28. Balakrishnan, V. *et al.* Expression and function of chloride transporters during development of inhibitory neurotransmission in the auditory brainstem. *J. Neurosci.* **23**, 4134–4145 (2003).
29. Kullmann, P.H., Ene, F.A. & Kandler, K. Glycinergic and GABAergic calcium responses in the developing lateral superior olive. *Eur. J. Neurosci.* **15**, 1093–1104 (2002).
30. Gao, B.X. & van den Pol, A.N. GABA, not glutamate, a primary transmitter driving action potentials in developing hypothalamic neurons. *J. Neurophysiol.* **85**, 425–434 (2001).
31. Ganguly, K., Schinder, A.F., Wong, S.T. & Poo, M. GABA itself promotes the developmental switch of neuronal GABAergic responses from excitation to inhibition. *Cell* **105**, 521–532 (2001).
32. Lauder, J.M., Liu, J., Devaud, L. & Morrow, A.L. GABA as a trophic factor for developing monoamine neurons. *Perspect. Dev. Neurobiol.* **5**, 247–259 (1998).
33. Kirsch, J. & Betz, H. Glycine-receptor activation is required for receptor clustering in spinal neurons. *Nature* **392**, 717–720 (1998).
34. Kotak, V.C., DiMattina, C. & Sanes, D.H. $GABA_B$ and Trk receptor signaling mediates long-lasting inhibitory synaptic depression. *J. Neurophysiol.* **86**, 536–540 (2001).
35. Chang, E.H., Kotak, V.C. & Sanes, D.H. Long-term depression of synaptic inhibition is expressed postsynaptically in the developing auditory system. *J. Neurophysiol.* **90**, 1479–1788 (2003).
36. Kakazu, H., Uchida, S., Nakagawa, T., Akaike, N. & Nabekura, J. Reversibility and cation selectivity of K^+-Cl^- cotransport in rat CNS Neurons. *J. Neurophysiol.* **84**, 281–288 (2000).
37. Nabekura J., Omura T. & Akaike N. Alpha2 adrenoceptor potentiates glycine receptor-mediated taurine response through protein kinase A in rat substantia nigra neurons. *J. Neurophysiol.* **76**, 2447–2454 (1996).
38. Matsubara, A., Laake, J.H., Davanger, S., Usami, S. & Ottersen, O. P. Organization of AMPA receptor subunits at a glutamate synapse: a quantitative immunogold analysis of hair cell synapses in the rat organ of Corti. *J. Neurosci.* **16**, 4457–4467 (1996).
39. Ottersen, O.P., Zhang, N. & Walberg, F. Metabolic compartmentation of glutamate and glutamine morphological evidence obtained by quantitative immunocytochemistry in rat cerebellum. *Neuroscience* **46**, 519–534 (1992).
40. Kaufman, D.L., McGinnis, J.F., Krieger, N.R. & Tobin, A.J. Brain glutamate decarboxylase cloned in lambda gt-11: fusion protein produces gamma-aminobutyric acid. *Science* **232**, 1138–1140 (1986).

Available online at www.sciencedirect.com
SCIENCE DIRECT®
Neuroscience Research 48 (2004) 211–220
Neuroscience Research
www.elsevier.com/locate/neures

Experience-dependent changes in intracellular Cl^- regulation in developing auditory neurons

Shumei Shibata[a], Yasuhiro Kakazu[a], Akihito Okabe[b], Atsuo Fukuda[b], Junichi Nabekura[a,*]

[a] *Department of Cellular and System Physiology, Graduate School of Medical Sciences, Kyushu University, Fukuoka 812-8582, Japan*
[b] *Department of Physiology, Hamamatsu University School of Medicine, Hamamatsu 420-3192, Japan*

Received 21 August 2003; accepted 29 October 2003

Abstract

A developmental change in GABA and glycine responses, from a depolarization to a hyperpolarization, have been reported for a range of CNS neurons, and has been demonstrated to be due to a developmental decrease in the intracellular Cl^- concentration ($[Cl^-]_i$). We examined $[Cl^-]_i$ in isolated rat lateral superior olive (LSO) neurons using patch-clamp recordings of glycine gated Cl^- currents and by measuring intracellular Cl^--fluorescence. In neurons from 14–16-day-old rats (P14–P16), which had previously received unilateral or bilateral cochlear ablations before the onset of hearing, there was no developmental decrease in $[Cl^-]_i$. No significant differences in $[Cl^-]_i$ were observed amongst rats with either ipsi- and contralateral ablations. Implanted strychnine pellets also prevented the decrease in $[Cl^-]_i$ in most neurons. In some of these neurons in which $[Cl^-]_i$ remained high, there was a lack of expression of the K^+–Cl^- cotransporter 2 (KCC2) mRNA. These results demonstrate that the developmental decrease in $[Cl^-]_i$ in LSO neurons is dependent on neuronal activity and that both GABAergic/glycinergic and glutamatergic afferent activity contribute to this maturation of the Cl^- regulatory mechanisms.

Keywords: Development; Ablation; KCC2; LSO; Auditory brainstem; Perforated-patch clamp; RT-PCR

1. Introduction

Many studies have indicated that excitatory neuronal circuits can be modified by sensory experiences (Wiesel and Hubel, 1963; Klinke et al., 1999; Rittenhouse et al., 1999; Di Cristo et al., 2001). There are also reports that inhibitory circuits are also adversely affected when sensory input is disrupted. In the visual and auditory systems, for example, deafferentation affects the development of appropriate inhibitory neuronal circuits (Hensch et al., 1998; Rajan, 1998; Mossop et al., 2000; Kapfer et al., 2002).

Deafferentation can also affect the subsequent properties of synaptic transmission across surviving synapses. At many immature synapses, activation of GABA or glycine receptor channels can evoke a membrane depolarization mediated by Cl^- efflux and resulting from a high intracellular Cl^- concentration ($[Cl^-]_i$) (Cherubini et al., 1991; Luhmann and Prince, 1991; Chen et al., 1996; Kaila, 1994; Rohrbough and Spitzer, 1996; Hollrigel and Soltesz, 1997). With maturation, $[Cl^-]_i$ becomes lower, and GABA and glycine typically cause a Cl^- influx and a hyperpolarization in mature neurons. Changes in $[Cl^-]_i$ throughout development are thought to be mediated by a developmental change in Cl^- transport proteins, which include the Na^+–K^+–Cl^- and K^+–Cl^- cotransporters (NKCC and KCC, respectively), and the Cl^-–HCO_3^- and Na^+–Cl^-–HCO_3^- exchangers (Kaila, 1994; Payne et al., 2003). Among these Cl^- transporters, a developmental up-regulation of the K^+–Cl^- cotransporter has been suggested to be responsible for the developmental decrease in $[Cl^-]_i$ (Rivera et al., 1999; Kakazu et al., 1999). In the inferior colliculus, bilateral cochlea ablations cause the reversal potential of evoked inhibitory postsynaptic currents (IPSCs) to remain at a more depolarized level (Vale and Sanes, 2000, 2002). The ablations also reduced the ability of neurons to transport Cl^-, although the levels of NKCC1 and KCC2 mRNA were unchanged (Vale et al., 2003). Bilateral ablations also reduced the postsynaptic conductance change associated with the IPSC, affected presynaptic

* Corresponding author. Tel.: +81-92-642-6090; fax: +81-92-642-6094.
E-mail address: nabekura@physiol2.med.kyushu-u.ac.jp (J. Nabekura).

0168-0102/$ – see front matter © 2003 Elsevier Ireland Ltd and The Japan Neuroscience Society. All rights reserved.
doi:10.1016/j.neures.2003.10.011

transmitter release and altered excitatory transmission in the inferior colliculus (Vale and Sanes, 2000, 2002). Just how deafferentiation leads to these changes is not clear.

The lateral superior olive (LSO) is the first auditory center involved in processing the different sound intensity experienced by the two ears (Sanes, 1993; Koyano and Ohmori, 1996). The LSO receives glutamatergic innervations directly from the ipsilateral cochlea nucleus, and GABA/glycinergic inputs from the contralateral cochlear nucleus via the medial nucleus of the trapezoid body (MNTB) (Grothe et al., 1994; Suneja et al., 1995; Vater, 1995; Winer et al., 1995; Kotak et al., 1998). Cochlea ablations in the first postnatal week have been shown to alter the morphology of LSO neurons and their inhibitory inputs (Sanes et al., 1992; Sanes and Chokshi, 1992). Contralateral cochlear ablation in immature gerbils, as well as in vivo application of strychnine, both of which should preferentially deafferentiate inhibitory inputs, disrupts the developmental refinement of LSO dendrites (Sanes and Takacs, 1993).

In this study, we investigate the effects of auditory experience on Cl^- homeostasis and KCC2 expression, in rat lateral superior olive neurons. We were particularly interested in whether just inhibitory input from the contralateral cochlea was sufficient to sustain the typical changes in $[Cl^-]_i$ and IPSCs seen during LSO development. We have also investigated whether there is any correlation between $[Cl^-]_i$ and the levels of KCC2.

2. Methods

2.1. Cochlea ablations and hearing tests

Bilateral and unilateral cochlear ablations were performed at P7. Rats were anesthetized with diethyl ether, and an incision was made just behind the pinna. Under a dissecting microscope, the middle ear cavity was exposed and the bony wall of the cochlea was identified. The cochlea was then carefully destroyed using a needle. Control sham-operated rats only received the incisions behind the pinna. After suturing the incision, we placed the animals on a heating pad until recovery from anesthesia was complete after which the pups were returned to their original cages and reared until P14.

At P14, the extent of hearing was tested by measurements of the auditory brainstem response (ABR) (Morishita et al., 2001). Briefly, rats were first anesthetized with injection of pentobarbital (60 mg/kg of body mass) and subcutaneous needle electrodes were placed at the vertex of the head, in the right and left retro-auricular region, and in the pre-sacral region of the rats. The sound stimulus was a 1 ms burst of 75 dB clicks presented at 5 kHz clicks (duration of each click was 0.1 ms), delivered to the rats through a probe designed to fit the external ear canal. For each recording condition, responses to 1000 bursts of clicks were averaged. All tests were performed in a soundproof room and the ABR was recorded with a SYNAX ER1100 system (NEC, Japan). The sound intensity through the probe was calibrated by a sound pressure meter (NL-04, Rion). The stimuli were delivered to control and test rats derived from the same litter.

2.2. Strychnine implants

To pharmacologically block glycinergic inputs, we implanted slow release strychnine pellets (i.e. strychnine-rearing). These strychnine pellets (0.05 mg 21-day-release, Innovative Research of America, Toledo, OH) were implanted subcutaneously at a posterior mid-dorsal location (Kotak and Sanes, 1996). Implantations were performed at P3, because rats suffered from general seizure when pellets were embedded at ages older than P5. After implantation, rats were returned to their litter.

2.3. Preparation of slices and acute dissociation of LSO neurons

Acute dissociation of central neurons was as described previously (Nabekura et al., 1996). Wister rats between P0–P3 or between P14–P16, either with or without cochlea ablation, or with strychnine pellets, were quickly decapitated under ether anesthesia and the brain was rapidly excised and immersed in ice-cold standard solution (below). Approximately 400 μm slices were cut using a vibratome (VT1000, Leica) and incubated in standard solution at room temperature for 1 h before a single slice was transferred to a petri dish and observed under the light microscope. Fine glass pipettes were placed on the surface of the LSO and gently vibrated so as to liberate single, mechanically dissociated LSO neurons. The dissociated LSO neurons were left for about 10 min to adhere to the bottom of the Petri dish before commencing electrophysiological recordings.

2.4. Solutions

The standard solution contained: NaCl, 150 mM; KCl, 5 mM; $MgCl_2$, 1 mM; $CaCl_2$, 2 mM; glucose, 10 mM and HEPES, 10 mM (pH = 7.4 with Tris-base). The artificial cerebrospinal fluid (ACSF) solution contained: NaCl, 124 mM; KCl, 5 mM; KH_3PO_4, 1.2 mM; $MgSO_4$, 1.3 mM; $CaCl_2$, 2.4 mM; glucose, 10 mM and $NaHCO_3$, 24 mM (pH = 7.45 with 95% O_2 and 5% CO_2). The pipette solution for the gramicidin perforated patch-clamp recordings contained: KCl, 150 mM; HEPES, 10 mM (pH = 7.2 with Tris-base). Gramicidin D, purchased from Sigma (USA), was dissolved in methanol as a 10 mg/ml stock solution, and this stock solution was diluted in the pipette solution to the given concentration. As the effectiveness of the diluted gramicidin stock solution gradually declined over time, it was prepared just before each experiment, and was only used for up to a maximum of 5 h.

2.5. Electrophysiological recordings

All electrical recordings utilized the gramicidin perforated patch-clamp technique. Membrane currents and voltages were continuously measured with a patch-clamp amplifier (EPC-7, List-Electronic), low pass filtered at 1 kHz (FV-665, NF Electronic Instruments), and monitored on both an oscilloscope (HS-5100A, Iwatsu) and a pen recorder (RECTI-HORIZ-8K21, Nihondenki San-ei). Data were simultaneously recorded on videotapes after digitalization (at 5 kHz) with a PCM processor (PCM 501 ESN, Nihon Koden). Patch pipettes were made from glass capillaries (outer diameter 1.5 mm) using a vertical pipette puller (PB-7, Narishige Scientific Instruments). The tip resistance was 4–8 MΩ. Voltage offsets were nulled before formation of the GΩ seal. After making contact with the cell surface, a GΩ seal was established by applying gentle suction to the patch pipette interior. After the cell attached configuration had been attained, the pipette potential was set to −50 and −10 mV hyperpolarizing step pulses were periodically delivered to monitor the access resistance. The access resistance typically reached a steady level below 20 MΩ within 40 min after making the GΩ seal. In all experiments, 75–80% series resistance compensation was employed. All experiments were carried out at 28–30 °C.

2.6. Drug application

External solutions were applied to single neurons using a "Y-tube" (Nabekura et al., 1993). Using this technique, solutions could be completely exchanged within 10–20 ms.

2.7. Drugs

Drugs used in the experiments were gramicidin D (Sigma, USA), glycine (Kanto, Japan; Tokyo Kasei, Japan), tetrodotoxin (TTX) (Sankyo, Japan). Final drug concentrations were made up from stock solutions just before use.

2.8. Optical imaging of intracellular Cl^-

The highly membrane permeant compound DiH-MEQ, was produced by reducing MEQ (Fukuda et al., 1998). Briefly, under protection from light, 5 mg of MEQ was dissolved in 100 μl of distilled water gassed with 100% N_2. The dissolved MEQ was reduced by addition of 15 μl of 12% $NaBH_4$. DiH-MEQ was extracted from the reaction mixture as a yellow organic layer with the aid of diethyl ether. This organic layer was dehydrated using 100 mg of $MgSO_4$ for 5 min, and the ether was then evaporated under a stream of 100% N_2 in a glass test tube. A portion of the organic extract was dissolved in 15 μl of ethyl acetate and added to the ACSF to yield a final concentration of 740 μM diH-MEQ.

Neurons were loaded with MEQ by incubating slices with diH-MEQ (740 μM) in ACSF for 60–90 min. DiH-MEQ is Cl^--insensitive, but it is readily loaded into cells where it is readily oxidized in the cytosol to form MEQ, which is both Cl^--sensitive and membrane impermeable (Biwersi and Verkman, 1991). The MEQ remains trapped in the cytosol for several hours. Pre-incubated slices were laid on the glass bottom of a submerged-type chamber, placed on a microscope stage and continuously perfused at a rate of 3–4 ml/min with ACSF.

For calibration of MEQ fluorescence we used ACSF solutions containing different Cl^- concentrations, in which the NaCl was replaced with equimolar concentrations of K gluconate.

MEQ fluorescence was excited at 330 nm (and emitted at 450 nm) using a Xenon arc lamp (75 W) and a band pass filter set. Fluorescence images were obtained using a CCD camera (Cool Snap cf., Roper Scientific) fitted to an upright microscope (DIA PHOT 300, Nikon). Images were digitized on-line, 128 frames being averaged to improve the signal to noise ratio. Data were analyzed using an image processor and data analysis software (MetaMorph/MetaVue, Roper Scientific). The apparent leakage and/or bleaching of MEQ under the recording conditions described here, was indicated by a gradual and linear decline in fluorescence, and was about 10–30% after 30 min. MEQ fluorescence was measured in the center of the soma of LSO neurons, once every 6–10 s. MEQ fluorescence was normalized to that initially observed, and plotted against time. Drugs were applied to the slices by bath perfusion.

2.9. Single-cell multiplex RT-PCR analysis

For harvesting cell cytoplasm for subsequent single-cell multiplex RT-PCR reactions, 10 μl of the standard pipette solution was injected into each patch-clamp pipette. After completion of the whole cell recording, mild suction was used to aspirate the contents of the cell into the recording pipette tip which were then expelled into a microfuge tube. The harvested cytoplasm was frozen with crushed dry ice and stored at −80 °C for a maximum of 2 days. Several target sequences were simultaneously amplified from a single cDNA synthesis by multiplex PCR with nested primers (below) and with two rounds of amplification. RT and first-round PCR reactions took place in the same tube using a OneStep RT-PCR kit (QIAGEN, GmbH). PCR analysis was carried out to determine the presence of β-actin and Cl^- transport proteins. For the initial RT-PCR, 10 μl of pipette solution containing the cell cytoplasm was placed into a thin-walled PCR tube and to this was added 10 μl of Qiagen OneStep RT-PCR buffer (5×), 2 μl of Qiagen OneStep RT-PCR enzyme mix, 0.4 mM of dNTP, 8 units of RNase inhibitor (Promega, Tokyo, Japan) and 0.6 μM of each primer, made up in buffer supplied by the manufacturer and added to give a final reaction volume of 50 μl. After the RT reaction at 50 °C for 30 min, the first-round PCR was subsequently performed in the same tube with a 15 min pre-incubation at 95 °C followed by 40 cycles of 30 s at 94 °C (denaturation),

30 s at 55 °C (annealing), 1 min at 72 °C (extension) in Program Temp Control System (PC-801, ASTEC Co. Ltd., Fukuoka, Japan). Subsequently, first-round PCR products were diluted 25-fold and re-amplified for 40 cycles (94 °C, 30 s; 60 °C, 30 s; 72 °C, 1 min) in separate reactions using the internal primer pairs for each template. The second-round PCR reaction was performed with 5 μl PCR buffer (10×), 3 mM $MgCl_2$, 0.2 mM of each dNTP (Amersham Bioscience, Tokyo, Japan), 1.25 units HotStar-Taq DNA polymerase (QIAGEN, GmbH) in the buffer supplied with enzyme and a reaction volume of 50 μl. The solution containing cDNA products was subjected to 10% acrylamide gel electrophoresis with ethidium bromide.

2.10. PCR primers

Nested primers used for the PCR analyses were selected based on the known rat cDNA or genomic sequences and are listed below. The outside primer pair is listed first in each case; the size of the final amplification product is shown in parentheses:

KCC2 (GenBank # U55816, Gillen et al., 1996), 5′-GATGAAGAAAGACCTGACCA-3′/5′-CTGGTTCAAGTTTTCCCACT-3′ and 5′-CATTCGGAGGAAGAATCCAG-3′/5′-TTTGTTCTTCTGAGCCGCTG-3′ (238 bp; 2935–3172 bp); β-actin (GenBank # V01217, Nudel et al., 1983), 5′-ACACGGCATTGTAACCAACT-3′/5′-CATTGCCGATAGTGATGACC-3′ and 5′-AGAAGATTTGGCACCACACT-3′/5′-CCATCTCTTGCTCGAAGTCT-3′ (435 bp).

3. Results

3.1. Developmental changes in $[Cl^-]_i$ in LSO neurons

In the present study, we used gramicidin perforated patch-clamp recordings from LSO neurons acutely dissociated from rats aged between P0–P2 and P14–P16. The gramicidin pore allows permeation of monovalent cations but does not allow anion permeation and hence the physiological $[Cl^-]_i$ is maintained (e.g., Kakazu et al., 1999). We measured the response to glycine at different membrane potentials and considered that E_{Gly} was close to the Cl^- equilibrium potential. The intracellular Cl^- concentration ($[Cl^-]_i$) could then be estimated using the Nernst equation (e.g., Kakazu et al., 1999). In neurons isolated from P0–P2 rats, with a large number of LSO neurons containing a relatively high $[Cl^-]_i$, there was a wide range of $[Cl^-]_i$, from between about 5–45 mM, with a mean value of 19.6 ± 1.8 mM (n = 37) (Fig. 1Aa). For almost all neurons from P16 rats, however, $[Cl^-]_i$ was below 10 mM with a mean value of 7.9 ± 0.3 mM, significantly lower than in the immature neurons ($P < 0.01$) (Fig. 1Ab). These results show that there is a fall in $[Cl^-]_i$ in LSO neurons during

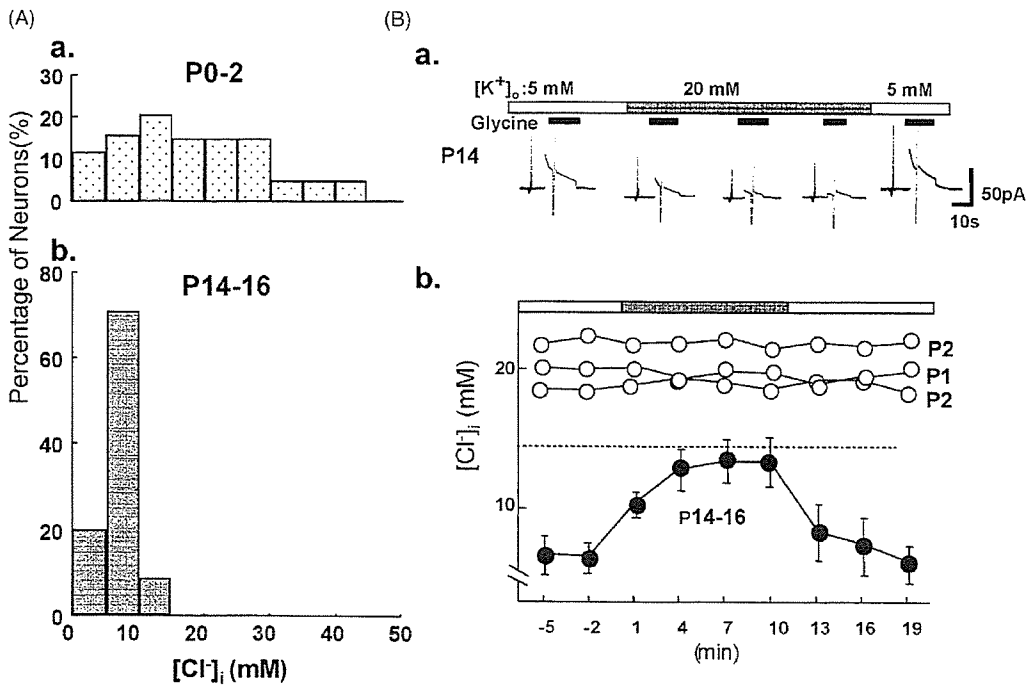

Fig. 1. Developmental increase in K^+-dependent Cl^- extrusion in LSO neurons. (A) Distribution of $[Cl^-]_i$ in LSO neurons, isolated from P0–P2 rats (upper, n = 37) and P14–P16 (lower, n = 37). Note the larger number of neurons with a relatively high $[Cl^-]_i$ in the P0–P2 neurons, while in P14–P16 neurons $[Cl^-]_i$ was typically below 10 mM. (B(a)) K^+-dependent Cl^- extrusion in mature LSO neurons at P14. V_H was −50 mV. An increase in $[K^+]_o$ from 5 to 20 mM abolished outward currents. The vertical current transients in current traces are in response to voltage ramps applied during the glycine response. (B(b)) $[Cl^-]_i$ in LSO neurons from P0–P2 (open circles) and from P14–P16 rats (filled circles, mean ± S.E.M., n = 6–12) before, during and after application of 20 mM $[K^+]$.

the first two postnatal weeks, and this results in a switch of glycine responses from excitatory to inhibitory.

3.2. Regulation of $[Cl^-]_i$ by cation-chloride cotransporters during development

Several studies have demonstrated that the K^+–Cl^- cotransporter (KCC) plays an important role in this developmental decrease in $[Cl^-]_i$, including in the LSO (Rivera et al., 1999; Kakazu et al., 1999). We also investigated the involvement of KCC in the present study, by altering its activity by manipulating the K^+ driving force across the plasma membrane. An increase in the extracellular K^+ concentration ($[K^+]_o$) is expected to cause a decrease in the ability of KCC to cotransport Cl^- and K^+ from inside cells. We monitored changes in $[Cl^-]_i$ by repetitively evoking glycinergic currents, which also causes some Cl^- loading into the cell at a V_H of −50 mV (e.g., Thompson and Gahwiler, 1989; Haas and Forbush, 1998; Kakazu et al., 2000; Ueno et al., 2002).

In neurons from P14–P16 rats, an increase in extracellular K^+ concentration ($[K^+]_o$) from 5 to 20 mM resulted in a gradual reduction in the amplitude of outwardly directed I_{Gly} evoked at a V_H of −50 mV (Fig. 1B). During perfusion with 20 mM $[K^+]_o$, $[Cl^-]_i$ was estimated from E_{Gly} to gradually increase to a significantly higher level than observed in the presence of 5 mM $[K^+]_o$ (Fig. 1B; $n = 5$; $P < 0.01$; paired t-test). At a V_H of −50 mV, I_{Gly} changed from an outward to an inward current in the presence of 30 mM $[K^+]_o$ (data not shown, see also Kakazu et al., 1999). After $[K^+]_o$ was returned from 20 to 5 mM, $[Cl^-]_i$ gradually recovered back to control values. This result indicates that $[K^+]_o$-dependent mechanism plays an important role in extruding Cl^- at P13–P15. In contrast, the initially higher $[Cl^-]_i$ in neurons from P0–P2 rats was less affected by a change in $[K^+]_o$ (Fig. 1Bb), indicating that this $[K^+]_o$-dependent $[Cl^-]_i$ regulation is not well developed in LSO neurons at this age (see also Kakazu et al., 1999).

3.3. Auditory activity alters the developmental changes in $[Cl^-]_i$

The hearing ability of rats was tested by recording the auditory brainstem response. Up until the age of P9, no ABR was observed in response to a 75 dB click, as previously reported (Geal-Dor et al., 1993). At P14 rats responded to the 75 dB click with a clear ABR (Fig. 2B, upper panel). In contrast, rats that received bilateral cochlear ablation at P7 showed no ABR at P14–P16 (Fig. 2B, middle panel). In rats who received a unilateral cochlear ablation at P7, the ABR in response to a click presented to the ear with cochlear ablation was diminished in amplitude, but the intact ear still showed a clear ABR (Fig. 2B, lower panel).

We next addressed the question whether auditory-dependent activity might influence the developmental decrease in the intracellular Cl^- concentration. Bilateral cochlear ablations or sham control operations were performed at P7. When neurons were subsequently isolated at P14, a significantly greater proportion of neurons from the cochlear ablation rats had a high $[Cl^-]_i$ when compared to those from the control rats ($P < 0.01$, Mann–Whitney test)(Fig. 3).

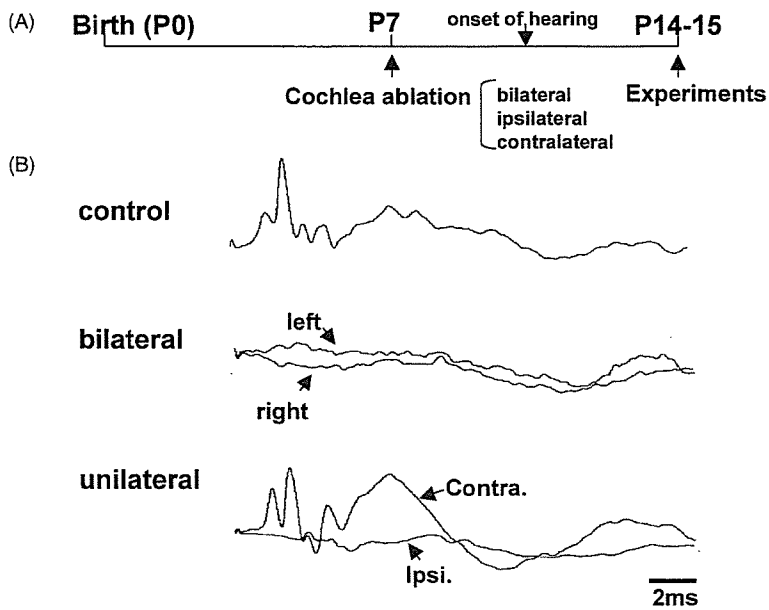

Fig. 2. Effects of cochlea ablation on the auditory brainstem responses. (A) Time line of experimental protocol. At P7, before the onset of hearing (P10–P12), bilateral or unilateral cochlea ablations, or sham control operations, were performed and auditory brainstem responses (ABR) were obtained at P14–P15. (B) ABRs recorded from control rats (upper trace), from rats with bilateral ablation in response to input to the left and right ears (center traces) and from rats with unilateral ablation in response to input to the ipsilateral and contralateral ears (lower traces). No response to sound stimuli applied to a cochlea-ablated ear were obtained.

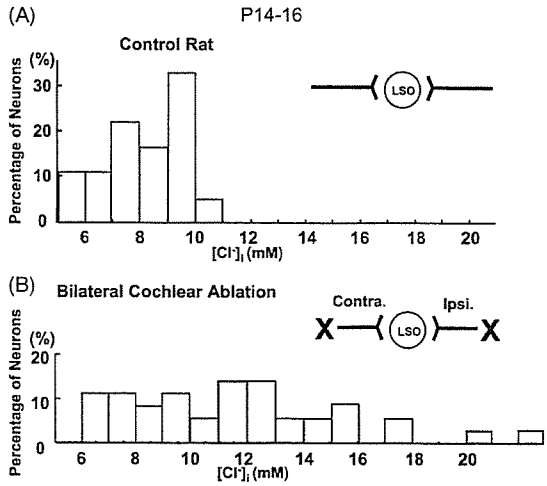

Fig. 3. Intracellular Cl^- concentration in LSO neurons from P14–P16 rats with sham and bilateral cochlear ablations performed at P7. Histograms showing the distribution of $[Cl^-]_i$ in LSO neurons from P14–P16 rats, with control (shame-operated, A) or bilateral cochlear ablations (B). $[Cl^-]_i$ was significant higher in the bilateral ablated rats, with a mean value of 11.6 ± 0.6 mM ($n = 32$) than in the sham control operated rats, with a mean value of 8.2 ± 0.2 mM ($n = 36$) ($P < 0.01$, Mann–Whitney test).

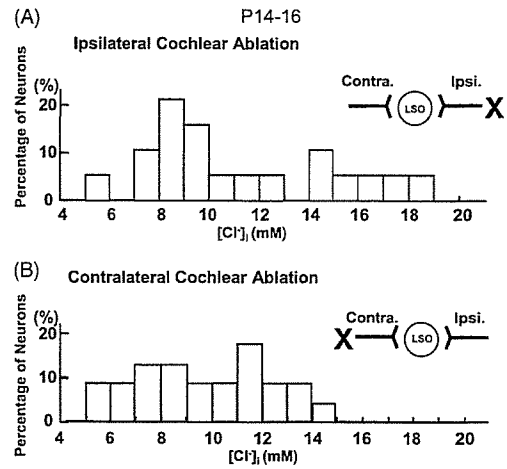

Fig. 4. Intracellular Cl^- concentration in LSO neurons from P14 rats with ipsi- or contralateral cochlear ablations performed at P7. Histograms showing the distribution of $[Cl^-]_i$ in LSO neurons from P14–P16 rats, with ipsilateral cochlea ablations (A) or contralateral cochlear ablations (B). For both groups, $[Cl^-]_i$ was significant higher (ipsi- 11.3 ± 0.9 mM, $n = 19$; contra- 9.8 ± 0.6 mM, $n = 23$) than in control (Fig. 3A) but there was no significant difference in the $[Cl^-]_i$ distribution between the ipsi- or contralateral ablations.

This indicates that the developmental decrease in intracellular Cl^- concentration is affected by auditory experience. On the other hand, $[Cl^-]_i$ in the bilateral ablation group (Fig. 3B) was significantly lower than $[Cl^-]_i$ in P0–P2 rats (Fig. 1Aa, $P < 0.05$), indicating that the developmental change in $[Cl^-]_i$ can proceed in the absence of auditory input and is accelerated by auditory experience.

We next investigated whether the ipsilateral auditory input (which sends glutamatergic afferents to the LSO) or the contralateral auditory input (involving GABAergic and glycinergic afferents) (Kotak et al., 1998) was predominantly responsible for the effects of the bilateral ablations. We performed unilateral cochlear ablations at P7 and recorded I_{GLY} in neurons isolated from the ipsilateral or contralateral LSO at P14–P16. Ablation of either the ipsilateral or contralateral cochlea both significantly affected the normal developmental decrease in $[Cl^-]_i$ ($P < 0.05$ contralateral ablation versus control; $P < 0.01$ ipsilateral ablation versus control) (Fig. 4). There appeared to be a larger number of neurons with $[Cl^-]_i > 15$ mM in neurons with an ablated ipsilateral input (Fig. 4), although there was no significant difference in the $[Cl^-]_i$ between neurons with ipsilateral, contralateral or bilateral ablations.

Finally, we examined the involvement of glycinergic neurotransmission in the developmental decrease in $[Cl^-]_i$ by using chronic in vivo blockade of glycine receptors with implanted strychnine pellets, which has previously been shown to disturb the morphological development of LSO neurons (Sanes and Chokshi, 1992). A significantly larger proportion of LSO neurons isolated from strychnine-reared rats at P14–P16 had a high $[Cl^-]_i$, when compared to neurons from control rats (Fig. 5A, $P < 0.05$). We also confirmed that strychnine-rearing attenuated the developmental decrease in $[Cl^-]_i$ using optical imaging with the Cl^- sensitive dye, MEQ (Fukuda et al., 1998). In LSO neurons in slices from P15 control rats, application of glycine elicited a decrease in MEQ fluorescence, indicating an increase in $[Cl^-]_i$ in response to glycine application (Fig. 5A). In contrast, application of glycine to LSO neurons in slices from strychnine-reared P15 rats, an increase in fluorescence was more typically seen in response to glycine, suggesting an efflux of Cl^- in response to glycine, consistent with an elevated initial $[Cl^-]_i$ (Fig. 5B). There was also typically a lower level of basal MEQ fluorescence in neurons from strychnine-reared rats, as compared to control neurons, which is also consistent with their higher basal $[Cl^-]_i$.

3.4. Developmental changes in KCC2 mRNA expression

Among the various KCC isoforms, KCC2 is neuron specific and changes in its function and/or expression have been shown to play a major role in the developmental decrease of $[Cl^-]_i$ (Rivera et al., 1999) and in the diversity of $[Cl^-]_i$ among neurons from various brain regions (Ueno et al., 2002). Therefore we performed single-cell RT-PCR to investigate any developmental change in KCC2 mRNA expression. We found that every LSO neuron isolated from P13–P16 rats expressed KCC2, while only two of seven LSO neurons from P0–P3 rats expressed KCC2. β-Actin was expressed at comparable levels in all neurons at both ages. In an additional set of experiments, we investigated whether there was a correlation between the $[Cl^-]_i$ concentration estimated during gramicidin perforated-patch recordings and

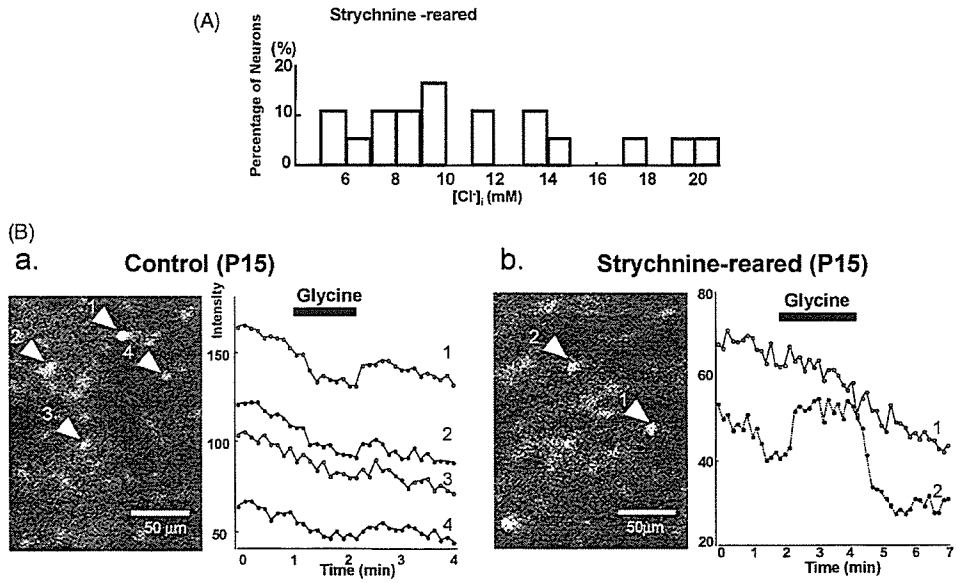

Fig. 5. Strychnine-reared rats maintain a high intracellular Cl^-. (A) Distribution of $[Cl^-]_i$ in neurons from P14–P16 rats in which strychnine pellets were implanted subcutaneously at a posterior mid-dorsal location at P3. Note the greater number of neurons with high $[Cl^-]_i$ (11.1 ± 1.1 mM, $n = 18$) than in the cochlear ablated experimental groups (Figs. 4 and 5A). (B) Effects of glycine on MEQ fluorescence in neurons from control (a) and strychnine-reared (b) rats. A decrease in fluorescence indicates an increase of $[Cl^-]_i$ and occurs in response to glycine in sham-operated control rat neurons (a). In contrast, in some neurons from strychnine-reared rats, there was an increase in fluorescence (i.e., a decrease in $[Cl^-]_i$) due to their higher resting $[Cl^-]_i$ (b).

KCC2 mRNA expression in the cytoplasmic constituents harvested from the same cell.

In three LSO neurons isolated from P0–P2 rats, KCC2 mRNA expression was only detected in the cell with the lowest $[Cl^-]_i$, which was about 14 mM (Fig. 6). All three neurons isolated from P14–P16 rats had $[Cl^-]_i$ about 10 mM or less, and all showed clear KCC2 mRNA expression (Fig. 6). We also performed combined RT-PCR and $[Cl^-]_i$ measurements on single LSO neurons isolated from P14–P16 rats with previous cochlear ablations. In two neurons that had received bilateral cochlea ablations, $[Cl^-]_i$ was maintained at a relatively high value and no KCC2 mRNA expression was observed (Fig. 6). In neurons from P14–P15 rats which had received either ipsilateral or contralateral ablations at P7, there was a good correlation between KCC2 mRNA expression and $[Cl^-]_i$, with only those neurons with $[Cl^-]_i$ below about 15 mM showing any KCC2 mRNA expression. This result suggests that activity in auditory afferents leads to an up-regulation of KCC2 expression, causing increased K^+-dependent Cl^- extrusion and a developmental decrease in $[Cl^-]_i$.

4. Discussion

In the present study, we have confirmed that there is a developmental decrease in $[Cl^-]_i$ in LSO neurons, and that this change is promoted by auditory-experience and seems to involve, at least partly, activation of glycine receptors.

4.1. Developmental changes of $[Cl^-]_i$ and Cl^- regulators

In many immature neurons, $GABA_A$ and glycine receptor-mediated responses are depolarizing and excitatory, and this is due to a high $[Cl^-]_i$ in immature neurons. While a developmental decrease in $[Cl^-]_i$ has been widely

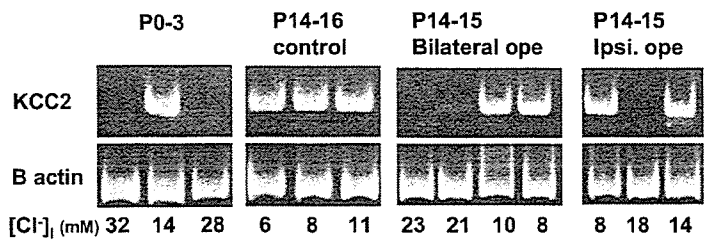

Fig. 6. KCC2 mRNA expression in single LSO neurons. Relationship between $[Cl^-]_i$ and the presence of KCC2 transcripts in individual LSO neurons from P0–P3 rats (left panel), from control P14–P16 rats (second panel from left) and from P14–P16 rats with previous cochlea ablations (right panels). KCC2 mRNA expression by single-cell RT-PCR was correlated with $[Cl^-]_i$ from the same cell. For LSO from P0–P3 rats, and for rats with previous bilateral, contralateral or ipsilateral ablations, KCC2 mRNA expression was only observed in those neurons in which $[Cl^-]_i$ was quite high. KCC2 expression was robust in all P14–P16 control neurons. β-Actin was expressed in all neurons.

reported in neurons, there is not complete consensus as to the underlying mechanisms, and particularly how KCC contributes. In the hippocampus, an up-regulation of KCC2 mRNA correlates well with the developmental decrease in $[Cl^-]_i$ (Rivera et al., 1999; Gulyas et al., 2001). Developmental increases in KCC2 expression levels have also been reported for the rat neocortex (Clayton et al., 1998; DeFazio et al., 2000) and the rat retina (Vu et al., 2000). Conversely, KCC2 expression levels are down-regulated following axotomy (Nabekura et al., 2002) and seizures (Reid et al., 2001); both of these events are also associated with increases in $[Cl^-]_i$. Difference in the levels of KCC2 expression between motor neurons and sensory neurons are also well correlated with their $[Cl^-]_i$ (Ueno et al., 2002). Hence a number of studies support an increase in KCC2 expression levels as a significant cause of developmental, pathological and random variations in neuronal $[Cl^-]_i$. On the other hand, however, KCC2 is reported to be already expressed in immature hippocampal neurons (Kelsch et al., 2001), in inferior colliculus neurons (Vale et al., 2003) and in LSO neuron (Balakrishnan et al., 2003) although, for reasons not yet clear, it does not seem to function effectively in extruding Cl^- at this developmental stage (see also Fig. 1, Kakazu et al., 1999). Our results suggest that KCC2 mRNA levels are too low to detect in many neonatal LSO neurons but becomes detectable in all neurons by 2 weeks after birth, a time when $[Cl^-]_i$ is reduced (Fig. 6A). Our results also indicate some heterogeneity in the developmental changes in Cl^- homeostasis, with KCC2 expression and low $[Cl^-]_i$ being observed in some neonatal neurons (Fig. 1).

Several reports indicate that neuronal activity is involved in the developmental and pathological regulation of Cl^-. In cultured hippocampal neurons, activation of $GABA_A$ receptors, but not glutamate receptor activation, promotes the increase in KCC2 mRNA expression and the associated decrease in $[Cl^-]_i$ (Ganguly et al., 2001). Deafferentation of gerbil inferior colliculus neurons (by bilateral cochlea ablation) at least partially prevents the typical developmental shift in the equilibrium potential of IPSCs to more hyperpolarized potentials (Vale and Sanes, 2000). The relatively depolarized IPSC reversal potential in the ablated gerbils was due to a lack of Cl^- transport function rather than any change in expression levels of KCC2 or NKCC1 (Vale et al., 2003). In our experiments, bilateral cochlear ablation also disrupted the normal developmental change in $[Cl^-]_i$, this is likely to be due to reduced LSO neuronal activity. Prior to the onset of hearing (which occurs around P10–P12 in rats), activation of Cl^- channels induces neuronal depolarization in the LSO (Kandler and Friauf, 1995), due to the high $[Cl^-]_i$ (Kakazu et al., 1999; Ehrlich et al., 1999). Our results are consistent with the hypothesis that this depolarizing afferent input, and the resulting membrane depolarization, are important in the development of KCC2 expression and Cl^- homeostasis. A similar disruption to Cl^- regulation was observed with either chronic strychnine treatment, ipsilateral ablation (causing predominantly a loss of glutamatergic afferents) or contralateral ablation (causing loss of GABAergic/glycinergic afferents). This suggests that both neurotransmitter systems can contribute to the changes in $[Cl^-]_i$, possibly reflecting their common ability to excite LSO neurons. Alternatively, ipsilateral ablation might also indirectly reduce GABAergic/glycinergic inputs to the LSO neurons, e.g., by decreasing excitatory input to local interneurons. This would be more consistent with the observation that activation of $GABA_A$ receptors, but not glutamate receptors, contributes to enhanced KCC2 expression (Ganguly et al., 2001).

4.2. Changes in the auditory brain stem with development

The LSO receives excitatory projections driven by sound input into the ipsilateral ear, and inhibitory projections driven by the contralateral ear. We show here that these inputs are required for development of Cl^- homeostasis. While this may be associated with inhibitory synaptic transmission, a number of other changes are occurring around the time when rats and gerbils acquire hearing ability (between P10 and P14). During the first 2 weeks after birth, massive synapse remodeling takes place within the LSO that is associated with changes in both morphology and function. Around the onset of hearing, there is a refinement of inhibitory afferent arborizations and the LSO dendrites that they innervate (Sanes and Friauf, 2000), including elimination of GABAergic/glycinergic inhibitory inputs (Kim and Kandler, 2003) and a change in the nature of the major inhibitory neurotransmitter from GABA to glycine (Kotak et al., 1998).

Several reports also suggest a role for afferent activity in these developmental changes. Removing the cochlear in the first neonatal week disturbs these refinements of axonal and dendritic morphology at inhibitory synapses (Sanes et al., 1992; Sanes and Chokshi, 1992). Contralateral cochlear ablation in immature gerbils, as well as in vivo application of strychnine, disturbs the refinement of dendritic spread of LSO neurons (Sanes and Takacs, 1993).

Our present study provides evidence that another crucial change in LSO physiology, i.e., alterations in Cl^- regulation, is also dependent on hearing experience. Sound afferents from the both the ipsilateral and contralateral ears are important in the maturation of $[Cl^-]_i$ homeostasis in LSO neurons, possibly due to their common depolarizing effect.

Acknowledgements

The authors wish to thank Dr. Andrew Moorhouse for language-editing this manuscript. This work was supported by Grants from the Ministry of Education, Science and Culture, Japan (Nos. 15016082, 15650076 and 15390065) to J.N.

References

Balakrishnan, V., Becker, M., Lohrke, S., Nothwang, H.G., Guresir, E., Friauf, E., 2003. Expression and function of chloride transporters during development of inhibitory neurotransmission in the auditory brainstem. J. Neurosci. 23, 4134–4145.

Biwersi, J., Verkman, A.S., 1991. Cell-permeable fluorescent indicator for cytosolic chloride. Biochemistry 30, 7879–7883.

Chen, G., Trombley, P.Q., van den Pol, A.N., 1996. Excitatory actions of GABA in developing rat hypothalamic neurones. J. Physiol. 494, 451–464.

Cherubini, E., Gaiarsa, J.L., Ben-Ari, Y., 1991. GABA: an excitatory transmitter in early postnatal life. Trends Neurosci. 14, 515–519.

Clayton, G.H., Owens, G.C., Wolff, J.S., Smith, R.L., 1998. Ontogeny of cation–Cl^- cotransporter expression in rat neocortex. Brain Res. Dev. Brain Res. 109, 281–292.

DeFazio, R.A., Keros, S., Quick, M.W., Hablitz, J.J., 2000. Potassium-coupled chloride cotransport controls intracellular chloride in rat neocortical pyramidal neurons. J. Neurosci. 20, 8069–8076.

Di Cristo, G., Berardi, N., Cancedda, L., Pizzorusso, T., Putignano, E., Ratto, G.M., Maffei, L., 2001. Requirement of ERK activation for visual cortical plasticity. Science 292, 2337–2340.

Ehrlich, I., Lohrke, S., Friauf, E., 1999. Shift from depolarizing to hyperpolarizing glycine action in rat auditory neurones is due to age-dependent Cl^- regulation. J. Physiol. 520 (Pt 1), 121–137.

Fukuda, A., Tanaka, M., Yamada, Y., Muramatsu, K., Shimano, Y., Nishino, H., 1998. Simultaneous optical imaging of intracellular Cl^- in neurons in different layers of rat neocortical slices: advantages and limitations. Neurosci. Res. 32, 363–371.

Ganguly, K., Schinder, A.F., Wong, S.T., Poo, M., 2001. GABA itself promotes the developmental switch of neuronal GABAergic responses from excitation to inhibition. Cell 105, 521–532.

Geal-Dor, M., Freeman, S., Li, G., Sohmer, H., 1993. Development of hearing in neonatal rats: air and bone conducted ABR thresholds. Hear Res. 69, 236–242.

Gillen, C.M., Brill, S., Payne, J.A., Forbush III, B., 1996. Molecular cloning and functional expression of the K–Cl cotransporter from rabbit, rat, and human. A new member of the cation-chloride cotransporter family. J. Biol. Chem. 271, 16237–16244.

Grothe, B., Schweizer, H., Pollak, G.D., Schuller, G., Rosemann, C., 1994. Anatomy and projection patterns of the superior olivary complex in the Mexican free-tailed bat, *Tadarida brasiliensis* mexicana. J. Comp. Neurol. 343, 630–646.

Gulyas, A.I., Sik, A., Payne, J.A., Kaila, K., Freund, T.F., 2001. The KCl cotransporter, KCC2, is highly expressed in the vicinity of excitatory synapses in the rat hippocampus. Eur. J. Neurosci. 13, 2205–2217.

Haas, M., Forbush III, B., 1998. The Na–K–Cl cotransporters. J. Bioenerg. Biomembr. 30, 161–172.

Hensch, T.K., Fagiolini, M., Mataga, N., Stryker, M.P., Baekkeskov, S., Kash, S.F., 1998. Local GABA circuit control of experience-dependent plasticity in developing visual cortex. Science 282, 1504–1508.

Hollrigel, G.S., Soltesz, I., 1997. Slow kinetics of miniature IPSCs during early postnatal development in granule cells of the dentate gyrus. J. Neurosci. 17, 5119–5128.

Kaila, K., 1994. Ionic basis of GABAA receptor channel function in the nervous system. Prog. Neurobiol. 42, 489–537.

Kakazu, Y., Akaike, N., Komiyama, S., Nabekura, J., 1999. Regulation of intracellular chloride by cotransporters in developing lateral superior olive neurons. J. Neurosci. 19, 2843–2851.

Kakazu, Y., Uchida, S., Nakagawa, T., Akaike, N., Nabekura, J., 2000. Reversibility and cation selectivity of the K(+)–Cl(−) cotransport in rat central neurons. J. Neurophysiol. 84, 281–288.

Kandler, K., Friauf, E., 1995. Development of glycinergic and glutamatergic synaptic transmission in the auditory brainstem of perinatal rats. J. Neurosci. 15, 6890–6904.

Kapfer, C., Seidl, A.H., Schweizer, H., Grothe, B., 2002. Experience-dependent refinement of inhibitory inputs to auditory coincidence-detector neurons. Nat. Neurosci. 5, 247–253.

Kelsch, W., Hormuzdi, S., Straube, E., Lewen, A., Monyer, H., Misgeld, U., 2001. Insulin-like growth factor 1 and a cytosolic tyrosine kinase activate chloride outward transport during maturation of hippocampal neurons. J. Neurosci. 21, 8339–8347.

Kim, G., Kandler, K., 2003. Elimination and strengthening of glycinergic/GABAergic connections during tonotopic map formation. Nat. Neurosci. 6, 282–290.

Klinke, R., Kral, A., Heid, S., Tillein, J., Hartmann, R., 1999. Recruitment of the auditory cortex in congenitally deaf cats by long-term cochlear electrostimulation. Science 285, 1729–1733.

Kotak, V.C., Korada, S., Schwartz, I.R., Sanes, D.H., 1998. A developmental shift from GABAergic to glycinergic transmission in the central auditory system. J. Neurosci. 18, 4646–4655.

Koyano, K., Ohmori, H., 1996. Cellular approach to auditory signal transmission. Jpn. J. Physiol. 46, 289–310.

Luhmann, H.J., Prince, D.A., 1991. Postnatal maturation of the GABAergic system in rat neocortex. J. Neurophysiol. 65, 247–263.

Morishita, H., Makishima, T., Kaneko, C., Lee, Y.S., Segil, N., Takahashi, K., Kuraoka, A., Nakagawa, T., Nabekura, J., Nakayama, K., Nakayama, K.I., 2001. Deafness due to degeneration of cochlear neurons in caspase-3-deficient mice. Biochem. Biophys. Res. Commun. 284, 142–149.

Mossop, J.E., Wilson, M.J., Caspary, D.M., Moore, D.R., 2000. Down-regulation of inhibition following unilateral deafening. Hear Res. 147, 183–187.

Nabekura, J., Ebihara, S., Akaike, N., 1993. Muscarinic receptor activation of potassium channels in rat dentate gyrus neurons. J. Neurophysiol. 70, 1544–1552.

Nabekura, J., Omura, T., Akaike, N., 1996. Alpha 2 adrenoceptor potentiates glycine receptor-mediated taurine response through protein kinase A in rat substantia nigra neurons. J. Neurophysiol. 76, 2447–2454.

Nabekura, J., Ueno, T., Okabe, A., Furuta, A., Iwaki, T., Shimizu-Okabe, C., Fukuda, A., Akaike, N., 2002. Reduction of KCC2 expression and GABAA receptor-mediated excitation after in vivo axonal injury. J. Neurosci. 22, 4412–4417.

Nudel, U., Zakut, R., Shani, M., Neuman, S., Levy, Z., Yaffe, D., 1983. The nucleotide sequence of the rat cytoplasmic beta-actin gene. Nucleic Acids Res. 11, 1759–1771.

Payne, J.A., Rivera, C., Voipio, J., Kaila, K., 2003. Cation-chloride co-transporters in neuronal communication, development and trauma. Trends Neurosci. 26, 199–206.

Rajan, R., 1998. Receptor organ damage causes loss of cortical surround inhibition without topographic map plasticity. Nat. Neurosci. 1, 138–143.

Reid, K.H., Li, G.Y., Payne, R.S., Schurr, A., Cooper, N.G., 2001. The mRNA level of the potassium-chloride cotransporter KCC2 covaries with seizure susceptibility in inferior colliculus of the post-ischemic audiogenic seizure-prone rat. Neurosci. Lett. 308, 29–32.

Rittenhouse, C.D., Shouval, H.Z., Paradiso, M.A., Bear, M.F., 1999. Monocular deprivation induces homosynaptic long-term depression in visual cortex. Nature 397, 347–350.

Rivera, C., Voipio, J., Payne, J.A., Ruusuvuori, E., Lahtinen, H., Lamsa, K., Pirvola, U., Saarma, M., Kaila, K., 1999. The K^+/Cl^- co-transporter KCC2 renders GABA hyperpolarizing during neuronal maturation. Nature 397, 251–255.

Rohrbough, J., Spitzer, N.C., 1996. Regulation of intracellular Cl^- levels by Na(+)-dependent Cl^- cotransport distinguishes depolarizing from hyperpolarizing GABAA receptor-mediated responses in spinal neurons. J. Neurosci. 16, 82–91.

Sanes, D.H., Markowitz, S., Bernstein, J., Wardlow, J., 1992. The influence of inhibitory afferents on the development of postsynaptic dendritic arbors. J. Comp. Neurol. 321, 637–644.

Sanes, D.H., Takacs, C., 1993. Activity-dependent refinement of inhibitory connections. Eur. J. Neurosci. 5, 570–574.

Sanes, D.H., 1993. The development of synaptic function and integration in the central auditory system. J. Neurosci. 13, 2627–2637.

Sanes, D.H., Friauf, E., 2000. Development and influence of inhibition in the lateral superior olivary nucleus. Hear Res. 147, 46–58.

Suneja, S.K., Benson, C.G., Gross, J., Potashner, S.J., 1995. Evidence for glutamatergic projections from the cochlear nucleus to the superior olive and the ventral nucleus of the lateral lemniscus. J. Neurochem. 64, 161–171.

Thompson, S.M., Gahwiler, B.H., 1989. Activity-dependent disinhibition. II. Effects of extracellular potassium, furosemide, and membrane potential on ECl^- in hippocampal CA3 neurons. J. Neurophysiol. 61, 512–523.

Ueno, T., Okabe, A., Akaike, N., Fukuda, A., Nabekura, J., 2002. Diversity of neuron-specific K^+–Cl^- cotransporter expression and inhibitory postsynaptic potential depression in rat motoneurons. J. Biol. Chem. 277, 4945–4950.

Vale, C., Sanes, D.H., 2000. Afferent regulation of inhibitory synaptic transmission in the developing auditory midbrain. J. Neurosci. 20, 1912–1921.

Vale, C., Sanes, D.H., 2002. The effect of bilateral deafness on excitatory and inhibitory synaptic strength in the inferior colliculus. Eur. J. Neurosci. 16, 2394–2404.

Vale, C., Schoorlemmer, J., Sanes, D.H., 2003. Deafness disrupts chloride transporter function and inhibitory synaptic transmission. J. Neurosci. 23, 7516–7524.

Vater, M., 1995. Ultrastructural and immunocytochemical observations on the superior olivary complex of the mustached bat. J. Comp. Neurol. 358, 155–180.

Vu, T.Q., Payne, J.A., Copenhagen, D.R., 2000. Localization and developmental expression patterns of the neuronal K–Cl cotransporter (KCC2) in the rat retina. J. Neurosci. 20, 1414–1423.

Wiesel, T.N., Hubel, D.H., 1963. Single-cell responses in striate cortex of kittens deprived of vision in one eye. J. Neurophysiol. 26, 1003–1017.

Winer, J.A., Larue, D.T., Pollak, G.D., 1995. GABA and glycine in the central auditory system of the mustache bat: structural substrates for inhibitory neuronal organization. J. Comp. Neurol. 355, 317–353.

THE JOURNAL OF BIOLOGICAL CHEMISTRY
Vol. 279, No. 48, Issue of November 26, pp. 50619–50629, 2004
Printed in U.S.A.

Membrane-embedded C-terminal Segment of Rat Mitochondrial TOM40 Constitutes Protein-conducting Pore with Enriched β-Structure*

Received for publication, July 29, 2004, and in revised form, September 1, 2004
Published, JBC Papers in Press, September 3, 2004, DOI 10.1074/jbc.M408604200

Hiroyuki Suzuki‡§, Tomoko Kadowaki§¶, Maki Maeda‡, Hiroyuki Sasaki‖, Junichi Nabekura, Masao Sakaguchi‡‡, and Katsuyoshi Mihara‡§§**

*From the ‡Department of Molecular Biology, Graduate School of Medical Science, Kyushu University, Fukuoka 812-8582, the ¶Department of Pharmacology, Graduate School of Dental Science, Kyushu University, the ‖Department of Molecular Cell Biology, Institute of DNA Medicine, The Jikei University School of Medicine, Tokyo 105-8451, the **Department of Cellular and System Physiology, Graduate School of Medical Sciences, Kyushu University, Fukuoka 812-8582, and ‡‡Graduate School of Life Science, University of Hyogo, Ako Hyogo 678-1297, Japan*

TOM40 is the central component of the preprotein translocase of the mitochondrial outer membrane (TOM complex). We purified recombinant rat TOM40 (rTOM40), which was refolded in Brij35 after solubilization from inclusion bodies by guanidine HCl. rTOM40 (i) consisted of a 63% β-sheet structure and (ii) bound a matrix-targeted preprotein with high affinity and partially translocated it into the rTOM40 pore. This partial translocation was inhibited by stabilization of the mature domain of the precursor. (iii) rTOM40 bound preprotein initially through ionic interactions, followed by salt-resistant non-ionic interactions, and (iv) exhibited presequence-sensitive, cation-specific channel activity in reconstituted liposomes. Based on the domain structure of rTOM40 deduced by protease treatment, we purified the elastase-resistant and membrane-embedded C-terminal segment (rTOM40(ΔN165)) as a recombinant protein with 62% β-structure that exhibited properties comparable with those of full-size rTOM40. We concluded that the membrane-embedded C-terminal half of rTOM40 constitutes the preprotein recognition domain with an enriched β-structure, which forms the preprotein conducting pore containing a salt-sensitive *cis*-binding site and a salt-resistant *trans*-binding site.

Mitochondrial precursor proteins synthesized in the cytosol are delivered to the preprotein translocase of the outer membrane (TOM[1] complex) where the precursors destined to the inner compartments are translocated across the membrane, and those destined to the outer membrane are sorted into the lipid bilayer of the membrane (1–6). In yeast, the ~400-kDa TOM holocomplex is composed of the import receptors Tom70, Tom20, and Tom22, the import channel Tom40 with a predicted β-barrel structure, Tom 5, which regulates precursor transfer from the receptor to the channel, and Tom6 and Tom7, which regulate channel assembly (4, 7). Tom22, Tom5, Tom6, and Tom7 are tightly associated with Tom40 and form the ~350-kDa TOM core complex (7–9). The TOM holocomplex and TOM core complex exhibit two to three ring structures with an ~20-Å diameter and voltage-dependent, cation-specific channel activity (3, 8–10). The oligomeric form of *Neurospora crassa* Tom40 (~350 kDa), purified after dissociating the TOM holocomplex with dodecylmaltoside, is mainly composed of a one-ring structure with a 20–30-Å diameter (10) and exhibits channel activity comparable with that of the TOM core and holocomplexes. Upon reconstitution into liposomes, they actively import preproteins destined for the outer membrane, intermembrane space, inner membrane, and matrix (3, 11). Purified recombinant yeast Tom40 reconstituted into liposomes forms a cation-selective and voltage-dependent high conductance channel with multiple conductance states, which specifically bind mitochondria-targeting sequences added to the *cis*-side of the membrane (12). Matrix-targeted precursors or synthetic presequence peptides added to the *cis*-side strongly reduced the channel open probability and increased the frequency of channel gating. In a recent report, site-specific cross-linking revealed that the Tom40 channel binds to unfolded segments of non-native proteins and prevents their aggregation. Furthermore, it has the capacity to sequester ~90 residues of unfolded or loosely folded preproteins (13).

Despite these advances, mechanism of preprotein recognition and sorting by the Tom40 machinery remains unclear, probably due, partly, to the difficulty in isolating Tom40 in the correctly folded and soluble form. In the present study, we expressed rat mitochondrial TOM40 (rTOM40) (14) in *Escherichia coli*, and we purified it from the inclusion bodies by solubilizing it in 6 M guanidine hydrochloride (GdnHCl) with subsequent refolding in the non-ionic detergent Brij35. The purified rTOM40 consisted of a ~63% β-structure and, when incorporated into liposomes, exhibited presequence-sensitive, cation-specific channel activity. A pull-down assay and surface plasmon resonance (SPR) revealed that purified rTOM40 directly bound loosely folded matrix-targeted preprotein, pSU9-DHFR, with high affinity (K_D range of 10^{-10}). Salt sensitivity of the binding indicated that rTOM40 recognized preproteins by two distinct sequential interactions: initial ionic interactions

* This work was supported by grants from the Ministry of Education, Science, and Culture of Japan (to M. S. and K. M.), from the Takeda Science Foundation, Core Research from Evolutional Science and Technology, and Specially Promoted Research from the Ministry of Education, Science, and Culture of Japan (to K. M.). The costs of publication of this article were defrayed in part by the payment of page charges. This article must therefore be hereby marked "*advertisement*" in accordance with 18 U.S.C. Section 1734 solely to indicate this fact.

§ Both authors contributed equally to this work.

§§ To whom correspondence should be addressed. Tel.: 81-92-642-6176; Fax: 81-92-642-6183; E-mail: mihara@cell.med.kyushu-u.ac.jp.

[1] The abbreviations used are: TOM, translocase of outer membrane; GdnHCl, guanidine hydrochloride; MPP, mitochondrial processing peptidase: pAd, preadrenodoxin; preSU9-DHFR, a construct in which a 1–69 segment of precursor for subunit 9 of *N. crassa* F_1-ATPase was fused to the N terminus of dihydrofolate reductase; SPR, surface plasmon resonance; HA, hemagglutinin; PMSF, phenylmethylsulfonyl fluoride; 2ME, 2-mercaptoethanol; rTOM40, recombinant rat TOM40; Ni-NTA, nickel-nitrilotriacetic acid; mAd, mature form of adrenodoxin.

followed by salt-resistant hydrophobic interactions. These sequential interactions drove partial translocation of preproteins and sequestration of the mitochondrial processing peptidase (MPP)-processing site of preproteins within the rTOM40 pore. We then narrowed the location of the β-structure-enriched channel domain to the membrane-embedded C-terminal half of rTOM40 (residues 166–361). Purified recombinant rTOM40(ΔN165) was in the oligomeric form of ~170-kDa, as assessed by gel filtration, and exhibited both structural and preprotein-binding characteristics almost identical to those of rTOM40.

EXPERIMENTAL PROCEDURES

Plasmid Constructions—For construction of the *E. coli* expression plasmid of rat TOM40, the 1086-bp cDNA encoding N-terminal His_6-tagged TOM40 was cloned into the NdeI-BamHI sites of pET28a (Novagen) to obtain pET28-NHis40 (14). The expression vector of rTOM40(ΔN165) was constructed as follows. A DNA fragment encoding His_6-TOM40(ΔN165) was prepared by PCR using pET28a-NHis40 as the template, and the following oligonucleotides as the primer: sense strand, 5′-GGGAATTCCATATGCACCAGCTGAGCCCAG GC-3′, and antisense strand, 5′-GCGGGATCCTCAGCCGATGGTGAG GCC AAA-3′. The NdeI and BamHI sites are underlined. The fragment was inserted into the NdeI-BamHI sites of pET28a to create pET28a-ΔN165. The expression vector for the N-terminal His_6-tagged TOM40-(1–165) was constructed as follows. A DNA coding for N-terminal His_6-tagged TOM40-(1–165) was amplified by PCR using pET28-NHis40 as the template and the following oligonucleotides as the primers: sense strand, 5′-GGGAATTCCATATGGGGAACGTGTTGGCTGCT-3′, and antisense strand, 5′-GCGGGATCCTCAGATGACCTGTGCATTGAG-3′. The NdeI and BamHI sites are underlined. The amplified fragment was inserted between the NdeI-BamHI sites of pET28a to create pET28a-(1–165).

Purification of rTOM40, rTOM40(ΔN165), and rTOM40-(1–165)—BL21(DE3)LysS cells harboring the expression plasmids for rTOM40, rTOM40(ΔN165), or rTOM40-(1–165) were cultured to A_{600} = 0.5, and protein expression was induced by 1 mM isopropyl 1-thio-β-D-galactopyranoside and cultured further for 3 h at 30 °C. The cells were suspended in the sonication buffer (50 mM Tris-HCl (pH 7.5) containing 250 mM NaCl, 1 mM EDTA, and 1 mM PMSF) and disrupted by sonication. For purification of rTOM40-(1–165), the soluble supernatant fraction obtained by ultracentrifugation was directly applied to a HiTrap chelating HP column (Amersham Biosciences). For purification of rTOM40 and rTOM40(ΔN165), the sonicated cell debris was washed with sonication buffer containing 1% Triton X-100, and the unsolubilized fraction was recovered by centrifugation. This step was repeated nine times, and the unsolubilized materials were washed once with 20 mM Tris-HCl (pH 7.5) containing 500 mM NaCl, 4 M urea, and 1 mM PMSF. After centrifugation, the obtained inclusion bodies were suspended in the lysis buffer (20 mM Tris-HCl buffer (pH 8.0), containing 0.5 M NaCl, 6 M guanidine HCl, 1 mM 2-mercaptoethanol (2ME), and 5 mM imidazole). The ultracentrifuged supernatant was passed through a HiTrap chelating HP column equilibrated with the lysis buffer. The column was extensively washed with washing buffer (20 mM Tris-HCl (pH 8.0) containing 0.5 M NaCl, 6 M urea, 1 mM 2ME, and 5 mM imidazole), and then the washing buffer was slowly exchanged (0.2 ml/min) by a concentration gradient from 0 to 100% of the refolding buffer (20 mM Tris-HCl (pH 8.0) containing 0.5 M NaCl, 0.5% Brij35, 1 mM 2ME). After the refolding step, rTOM40 or rTOM40(ΔN165) was eluted by 20 mM Tris-HCl buffer (pH 8.0) containing 0.5 M NaCl, 0.5% Brij35, 1 mM 2ME, and 300 mM imidazole. The eluted fraction was applied to a Mono-S column equilibrated with 20 mM phosphate buffer (pH 6.5) containing 0.5% Brij35, and eluted by a 0 to 1 M NaCl concentration gradient in the same buffer. The eluted proteins were dialyzed against 20 mM sodium phosphate buffer (pH 7.0) containing 0.5% Brij35. Approximately 5 mg of rTOM40 or rTOM40(ΔN165) was obtained in high purity from ~15 g (wet weight) of *E. coli* cells.

Preparation of Elastase Fragments of rTOM40 for the N-terminal Sequencing—The reaction mixture (50 μl) containing 3 μg of rTOM40 and elastase (2 μg/ml) was incubated at 0 °C for 30 min. The protein fragments were recovered by trichloroacetic acid precipitation and separated by SDS-PAGE. The fragments were transferred to polyvinylidene difluoride membrane followed by Ponceau S-staining. The stained bands were cut out and subjected to protein sequencing.

Preparation of Proteoliposomes—Preparation of proteoliposomes containing rTOM40 was essentially according to the method described by Jackson and Litman (15). Briefly, 1.2 mg of L-α-phosphatidylcholine and 0.8 mg of L-α-phosphatidylethanolamine in chloroform were mixed in a test tube, and the solvent was evaporated by flushing with N_2. One milliliter of 50 mM Tris-HCl buffer (pH 7.5) containing 0.5% Brij35 and 20 μg of rTOM40 was added to the tube, vortexed, and incubated on ice for 4 h with intermittent mixing. After incubation, the reaction mixture was diluted in 50 ml of 50 mM Tris-HCl buffer (pH 7.5) containing 50 mM sodium acetate. The reaction mixture was then dialyzed against 5 liters of 10 mM Tris-HCl buffer (pH 7.5) containing 0.15 M NaCl and 20 g of Bio-Beads SM-2 (Bio-Rad). The dialysate was concentrated using a membrane filter. Approximately 80% of the obtained proteoliposomes assumed unilamellar vesicles with ~0.1 μm diameter.

Preparation of Mitochondria from HeLa Cells Expressing the Epitope-tagged rTOM40—HeLa cells were transfected with N-terminal His_6-tagged rTOM40 or C-terminal HA-tagged rTOM40 using FuGENE 6 (Roche Applied Science) and cultured for 24 h. The cells were collected and homogenized in the homogenization buffer (10 mM Hepes-KOH buffer (pH 7.4), containing 0.22 M mannitol, 0.07 M sucrose, and 1 mM PMSF) by passing them through a 27-gauge needle 20 times using a syringe. The homogenate was centrifuged at 600 × *g* for 5 min, and the supernatant was then centrifuged at 6000 × *g* for 10 min to obtain the mitochondrial fraction.

Measurement of Channel Activity—Electrical measurements were performed with nystatin-perforated patch recordings applied on lipid bilayer vesicles containing rTOM40. SCC1–19 (10 μM) dissolved in the perfusate was applied using the Y-tube method, which allowed the external solution to be exchanged within 20 ms (16). The resistance between the patch pipette and the reference electrode in the external solution was 10–12 megohms. Ionic currents were measured with a patch clamp amplifier (EPC-7, List-Medical, Germany) and low pass filtered at 1 kHz (E-3210A, NF Electronic Instruments, Japan). All experiments were performed at room temperature. The composition of the pipette solution was 100 mM KCl, 50 mM potassium methane sulfonate, and 10 mM Hepes (pH 7.2). The external solution contained 150 mM KCl, 10 mM Hepes (pH 7.2), and 1 mM $CaCl_2$. In some experiments, the reversal potentials were obtained as the membrane potential at which the current responses to ramp voltage steps from −100 mV to +100 mV with and without SCC1–19 intersected with each other. The presence of the TOM40 pore was verified by measuring release of [^{14}C]sucrose from the proteoliposomes containing rTOM40 or rTOM40(ΔN165). The assay was carried out essentially as described by Zalman *et al.* (17) using [^{14}C]sucrose and [^{3}H]dextran (mean M_r, 70,000) as the permeable and impermeable substrates, respectively, except that rTOM40, rTOM40(ΔN165), rTOM40-(1–165), or lactate dehydrogenase, in lieu of mitochondrial outer membrane, was reconstituted into asolectin liposomes. The reaction mixture was passed through a Sepharose CL-4B column (0.9 × 9.5 cm) equilibrated with 10 mM Hepes-KOH buffer (pH 7.4) containing 100 mM NaCl, 0.1 mM $MgCl_2$, and 3 mM NaN_3. 0.3-ml fractions were collected and assayed for radioactivity by using a liquid scintillation counter. Membrane vesicles were eluted in fractions 6–7 (Fig. 7*B*).

Isolation of Proteoliposomes by Centrifugal Floatation—After reconstitution of proteoliposomes, the reaction mixture was adjusted to 1.6 M sucrose, placed under the layers of 1.25 M and 0.25 M sucrose, and centrifuged in a Hitachi RP-S120AT3 rotor at 100,000 rpm for 90 min. Proteoliposomes floated to the 0.25 and 1.25 M sucrose layers were recovered and analyzed by SDS-PAGE.

Binding Assay of Preproteins to rTOM40, rTOM40(ΔN165), or rTOM40-(1–165) by Co-precipitation—The mixture containing 1 μg of pAd and the indicated amounts of rTOM40, rTOM40(ΔN165), or rTOM40-(1–165) in 200 μl of the binding buffer (20 mM Hepes-KOH buffer (pH 7.4) containing 0.1% Brij35, and 50 mM NaCl) was incubated at 30 °C for 30 min. The reaction mixture was centrifuged at 45,000 rpm for 5 min. The obtained supernatant was mixed with 30 μl (50% slurry) of TALON metal affinity resin (Clontech) and incubated at 4 °C for 1 h. The beads were washed with the binding buffer, and the bound proteins were analyzed by SDS-PAGE and subsequent immunoblotting using anti-adrenodoxin IgG.

Protection of the MPP-processing Site of pAd by rTOM40 or rTOM40(ΔN165)—Binding of pAd to rTOM40, rTOM40(ΔN165), or rTOM40-(1–165) and isolation of the complex by TALON beads were performed as described above. The isolated beads were suspended in 25 μl of the binding buffer, and the suspension was then incubated with 3 μg of yeast recombinant MPP in the presence of 2 mM MnCl2 at 30 °C for 30 min. The reaction was terminated with the sample loading buffer and analyzed by SDS-PAGE and subsequent immunoblotting using anti-adrenodoxin IgG.

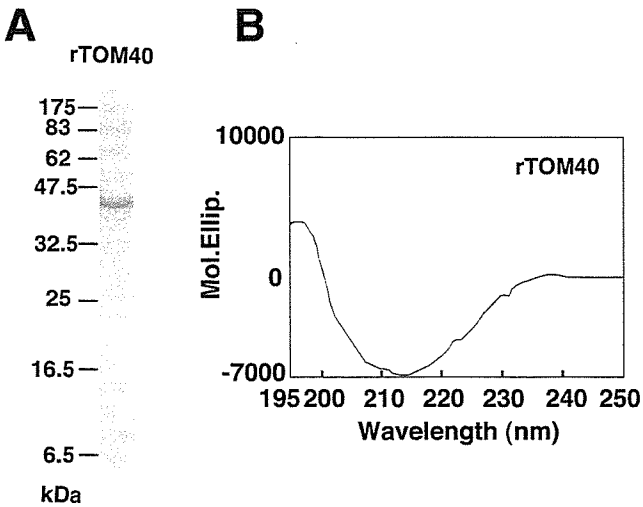

FIG. 1. **Structural characteristics of rTOM40.** *A*, SDS-PAGE profile of purified rTOM40. *B*, CD spectrum of rTOM40.

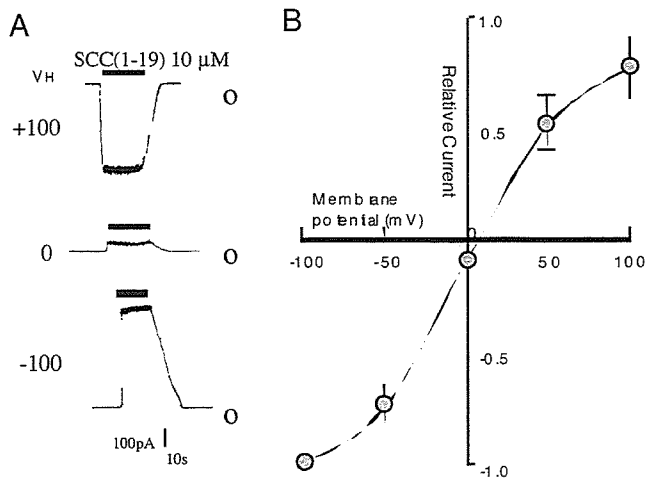

FIG. 2. **Kinetics and reversal potential of presequence peptide-sensitive current of the rTOM40 channel.** *A*, the presequence peptide-induced shift of the current level. *B*, relative current as a function of applied membrane potential. Electrical measurements were performed as described under "Experimental Procedures."

CD Spectrum Measurement—CD spectra of rTOM40, rTOM40(ΔN165), and rTOM40-(1–165) were measured in 10 mM Tris-HCl buffer (pH 7.4) containing 0.5% Brij35 at 25 °C using a JASCO J-720 spectropolarimeter and a cuvette with a 1-mm light-path. Each spectrum represents an average of five scans from 195 to 250 nm at 0.1-nm intervals. The base line was established by subtracting the spectrum of the buffer alone. Analysis of the secondary structure was performed using the method of Reed and Reed (18).

Surface Plasmon Resonance Measurements—The SPR measurements were performed at 25 °C with a Biacore 3000 (Biacore AB). Purified rTOM40, rTOM40(ΔN165), or rTOM40-(1–165) was immobilized onto the sensor chip CM5 by amine-coupling according to the manufacturer's protocol. Briefly, the coupling was performed in 10 mM sodium acetate buffer (pH 6.5) at a protein concentration of 10 μg/ml. The level of immobilization typically corresponded to 2000 resonance units, which corresponded to ~2 ng of protein/mm^2 (Fig. 6, *A–D*). In Fig. 6*E*, rTOM40 was immobilized to the chip at 22,000 resonance units (corresponding to ~22 ng of protein/mm^2). Binding analyses were performed in 20 mM Hepes-KOH buffer (pH 7.4) containing 150 mM NaCl and 0.05% Brij35 (running buffer) at a flow rate of 20 μl/min. The sensor chip surface was regenerated by 50 mM HCl. Binding curves were analyzed using BIA-Evaluation software (version 3.2). The kinetic data fitting was performed using a Langmuir 1:1 binding model.

RESULTS

Purification of Rat TOM40—N-terminal His_6-tagged rTOM40 expressed in *E. coli* as inclusion bodies was solubilized by 6 M GdnHCl, applied to a Ni-NTA affinity column, and subjected to a refolding reaction by exchanging GdnHCl slowly with Brij35. rTOM40 was then eluted by imidazole and subjected to Mono-S column chromatography. Purified rTOM40 (Fig. 1*A*) was eluted through a Superose 6 column with a peak at ~250 kDa, although with a rather broad elution profile (see Fig. 5*B*).

Secondary Structure of rTOM40—A CD spectrum of rTOM40 in 0.5% Brij35 had a minimum value at 213 nm, crossover of the base line at 201 nm, and zero ellipticity at a wavelength 235 nm (Fig. 1*B*). The secondary structure of rTOM40 estimated from the CD spectrum using the program of Reed and Reed (18) comprised 62.9% β-sheet, 10.0% α-helix, 5.9% turn, and 21.1% random structures in the protein. The content of the β-sheet structure of rTOM40 was comparable with that of recombinant *Saccharomyces cerevisiae* Tom40 (>60%) purified from inclusion bodies after solubilization with 8 M urea and either reconstituted into liposomes or solubilized in Mega9, although the CD spectra were distinct (12). The secondary structure of rTOM40 was significantly different from that of the oligomeric form of *N. crassa* Tom40, which was purified after dissociation of the purified TOM complex with octyl glucoside (less β-sheet, ~31%; more α-helix, 30%) (10). The reason for this structural difference between rat and *N. crassa* Tom40 is not known.

Channel Properties of rTOM40—The purified TOM holocomplex, TOM core complex, oligomeric *N. crassa* Tom40 isolated from the purified TOM core complex, and recombinant Tom40 of *S. cerevisiae* form cation-selective high conductance channels when incorporated into lipid membranes and the presequence peptide block the channel in a voltage-dependent manner (3, 8, 10, 12, 19). We therefore examined whether purified rTOM40 was correctly folded to exhibit channel activity. rTOM40 was incorporated into unilamellar ~0.1-μm-diameter liposomes, and electrical measurements were performed with nystatin-perforated patch recordings. A functional presequence peptide SCC1–19 (10 μM) (20) induced an immediate outward shift of current at a holding potential of −100 mV in less than 1 s (Fig. 2). During SCC1–19 application, there was no desensitization of the current but current noise increased. The current returned to base line within 10 s upon washing out the presequence peptide. Less hyperpolarization of the membrane reduced SCC1–19-induced current amplitude and a positive membrane potential reversed the direction of SCC1–19-induced current inward. The reversal potential of SCC1–19-induced current was 8.3 ± 3.2 mV (mean ± S.E., n = 5). This result suggested that the lipid bilayer with rTOM40 contains cation-permeable ion channels that are rapidly and reversibly blocked by the presequence peptide.

Binding of Matrix-targeted Preproteins to Purified rTOM40—Confirming that recombinant rTOM40 had refolded to constitute a dominant β-sheet structure and to exhibit channel activity, we examined its interaction with matrix-targeted preproteins. Recombinant preadrenodoxin (pAd) (21) was incubated with rTOM40 (N-terminal His_6-tagged), and rTOM40 was recovered with nickel resin. Immunoblot analysis with anti-adrenodoxin antibody revealed that pAd was recovered to the nickel resin depending on the amount of rTOM40 added to the reaction mixture (Fig. 3*A*). As a control, the mature form of adrenodoxin (mAd) did not bind to rTOM40 (data not shown). The interaction between rTOM40 and pAd was sensitive to NaCl, and the interaction was almost completely abolished by 500 mM NaCl (Fig. 3*B*). The pAd·rTOM40 complex, once formed, was stable in high salt (Fig. 3*B*, *Af* in the *lower panel*). These results suggested that the preprotein initially binds to rTOM40 mainly through ionic interactions, which is followed

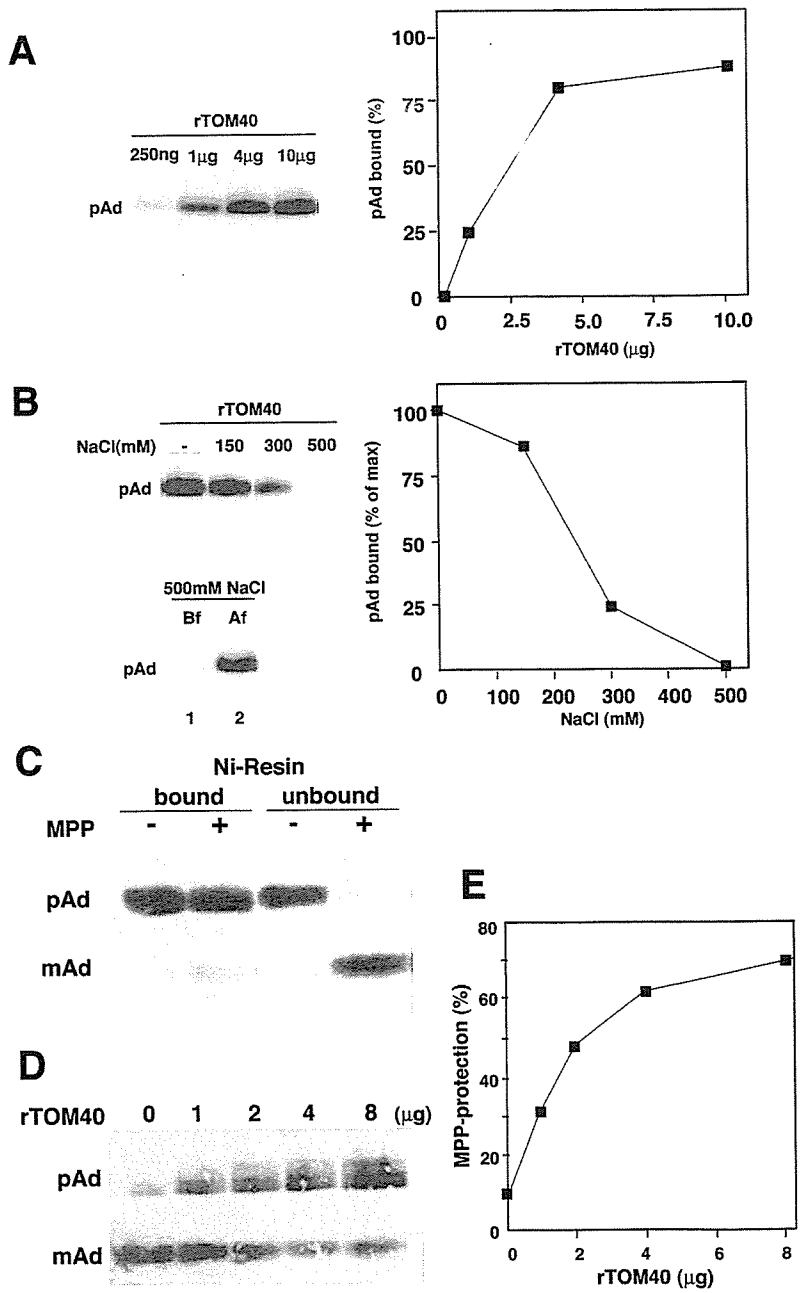

FIG. 3. **Recognition of preprotein by purified rTOM40.** *A*, binding of pAd to rTOM40 as measured by pull-down assay. pAd (1 μg) was incubated with the indicated amounts of rTOM40 (N-terminal His_6-tagged), and then the reaction mixtures were subjected to pull-down reaction by Ni-NTA beads. The recovered pAd·rTOM40 complex was subjected to SDS-PAGE followed by immunoblotting using anti-adrenodoxin antibodies and subsequent image analysis by a LAS1000 *plus* (Fuji Film Co.). The band intensities were calculated by setting the total pAd signal to 100% (shown in the *right panel*). *B*, salt sensitivity of the pAd·rTOM40 complex. The binding assay was performed as in *A* using 5 μg of rTOM40 in the presence of the indicated concentrations of NaCl. In the *lower panel*, the pAd·rTOM40 complex formed after 30 min of incubation was incubated with 500 mM NaCl (*Af*) and then subjected to the pull-down assay as in *A*. In a separate experiment, pAd and rTOM40 were incubated in the presence of 500 mM NaCl (*Bf*) followed by the pull-down assay. The quantified results are shown in the *right panel*. *C*, sequestration of the MPP-processing site of pAd within the rTOM40 molecule. pAd (1.4 μg) and rTOM40 (3.8 μg) were incubated in 50 μl at 30 °C for 30 min. The reaction mixtures were then incubated with Ni-NTA beads to separate into pAd (*unbound*) and the pAd·rTOM40 complex (*bound*). Both fractions were then incubated with (+) or without (−) MPP at 30 °C for 30 min, and the reaction mixtures were analyzed by SDS-PAGE and subsequent immunoblotting with anti-adrenodoxin antibodies. *D*, dose-dependent sequestration of the MPP-processing site of pAd by rTOM40. pAd (1 μg) and the indicated amounts of rTOM40 were incubated at 30 °C for 30 min. The reaction mixtures were then incubated with MPP at 30 °C for 30 min, which were subjected to SDS-PAGE and subsequent image analysis. The protection efficiency (%) was calculated as the ratio of pAd to pAd *plus* mAd, and shown in *E*.

by the other interactions involving hydrophobic interactions. The so-called "*cis*-binding sites" or "*cis*-sites" of mitochondria or mitochondrial outer membranes, which are located in the protease-sensitive surface receptors Tom20 and Tom22, are sensitive to salt concentrations as low as 100 mM (22–26). Therefore, the "*cis*"-site of TOM40 involved in the initial precursor recognition binds preproteins through stronger ionic interactions than that for the *cis*-binding site of the mitochondrial outer membrane. Stan *et al.* (27) demonstrated that the isolated *N. crassa* TOM holocomplex and the proteinase K-treated core not only bind pSU9-DHFR but protect the precursor from cleavage by MPP, indicating partial translocation of the precursor protein into the TOM complex and that the MPP cleavage site is protected by the TOM complex against MPP. Because this MPP protection is a suitable criterion to assess Tom40 function, we examined MPP protection with rTOM40. Recombinant pAd was incubated with rTOM40 and then the pAd·rTOM40 complex was isolated using nickel resin, which was then subjected to MPP digestion. As shown in Fig. 3*C*, the pAd recovered as the complex with rTOM40 was protected against MPP, whereas unbound pAd was efficiently processed. This protection occurred as a function of the amount of rTOM40 (Fig. 3, *D* and *E*), and the reaction was essentially saturated by 4–8 μg of rTOM40 per 1 μg of pAd (roughly calculated, ~2–4 mol of rTOM40/mol of pAd, assuming the molecular size of rTOM40 and pAd to be 38 and 20 kDa, respectively). The rTOM40-dependent MPP protection was also observed for pSU9-DHFR (data not shown). Therefore, recombinant rTOM40 had properties similar to those of the isolated *N. crassa* TOM holocomplex or the proteinase K-treated core, which is composed solely of the oligomeric form of Tom40 (27). The TOM core complex was unable to partially translocate the preprotein unless phospholipids from the mitochondrial outer membrane were supplied externally (27). Because phospholipid P_i was not detected in our rTOM40 preparation (data not shown), rTOM40 seemed to have folded correctly in Brij35 during the

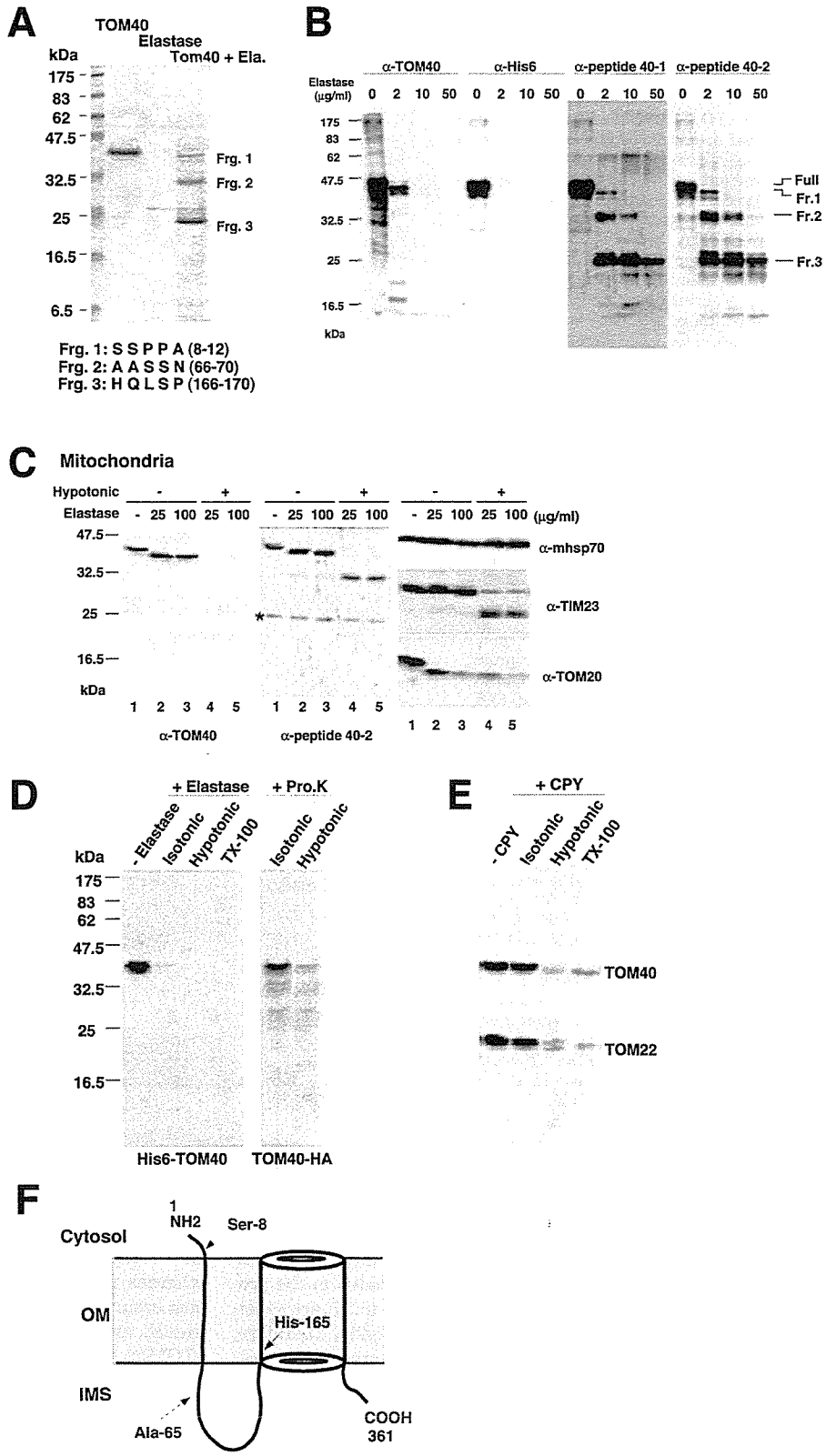

FIG. 4. **Domain structure and membrane topology of rTOM40.** *A*, elastase (*Ela*) digestion of rTOM40. rTOM40 (3 μg) was digested with 2 μg/ml elastase in 50 μl at 0 °C for 30 min. The reaction mixture was trichloroacetic acid-precipitated and analyzed by SDS-PAGE and subsequent Coomassie Brilliant Blue staining. *B*, recognition of the elastase-produced fragments of rTOM40 by various antibodies. rTOM40 (3 μg) was digested in 50 μl with the indicated concentrations of elastase at 0 °C for 30 min. The reaction mixtures were trichloroacetic acid-precipitated, and the precipitates were solubilized in the loading buffer, divided into 4 aliquots, and analyzed by SDS-PAGE and subsequent immunoblotting using the indicated antibodies. *C*, elastase susceptibility of endogenous rTOM40 in the mitochondrial outer membrane. Mitochondria (50 μg/100 μl) were digested with the indicated concentrations of elastase at 0 °C for 30 min under isotonic (−) or hypotonic (+) conditions. The reaction mixtures were trichloroacetic acid-precipitated and subjected to SDS-PAGE and subsequent immunoblotting using the indicated antibodies. *Asterisk*, nonspecific band. *D*, membrane topology of the N- and C-terminal ends of rTOM40 in the outer membrane as probed by elastase and proteinase K (*Pro.K*). Mitochondria (10 μg/100 μl) harboring either N-terminal His_6-tagged rTOM40 (His_6-TOM40) or C-terminal HA-tagged rTOM40 (TOM40-HA) were treated with or without 100 μg/ml elastase or 100 μg/ml proteinase K at 0 °C for 30 min under the indicated conditions. The trichloroacetic acid-precipitates were resolved by SDS-PAGE and analyzed by immunoblotting using the antibodies against His_6 or HA. *TX-100*, Triton X-100. *E*, topology of the C-terminal end of rTOM40 in the mitochondrial outer membrane as probed by carboxypeptidase Y (*CPY*). Mitochondria (50 μg/100 μl) were treated with 5 μg/ml carboxypeptidase Y at 30 °C for 30 min under the indicated conditions. The reaction mixtures were analyzed by SDS-PAGE and subsequent immunoblotting using the indicated antibodies. *F*, schematic representation of the topology of rTOM40 in the mitochondrial outer membrane. The β-structure-enriched C-terminal half is shown as the cylindrical structure. The sites Ala^7–Ser^8 and Ala^{65}–Ala^{66} are accessible to elastase from outside mitochondria and from the intermembrane space, respectively, whereas Ile^{165}–His^{166}, which is accessible to elastase in the purified rTOM40, is resistant in the outer membrane to elastase treatment from either side of the membrane. The segment 1–165 should span the membrane at least once, although the detailed membrane disposition of this segment is not known. *OM*, outer membrane; *IMS*, intermembrane space.

purification process to acquire the activity of partial translocation of preproteins even in the absence of phospholipids.

Domain Structure of rTOM40 and Its Membrane Topology—We then probed the domain structure of purified rTOM40 using protease digestion. Elastase (2 μg/ml) treatment of rTOM40 at 0 °C for 30 min produced at least three distinct fragments (Fig. 4*A*). Fragments 1 and 2 were formed transiently, and fragment 3 was formed stably. These fragments were detected even after 50 μg/ml elastase digestion (see Fig. 4*B*). N-terminal amino acid sequencing revealed that fragments 1–3 had lost residues 1–7, 1–65, and 1–165, respectively. The antibodies against rTOM40 (α-TOM40) recognized only fragment 1, whereas two antibodies raised against the synthetic peptides corresponding to the regions near the C terminus (residues 323–345: peptide

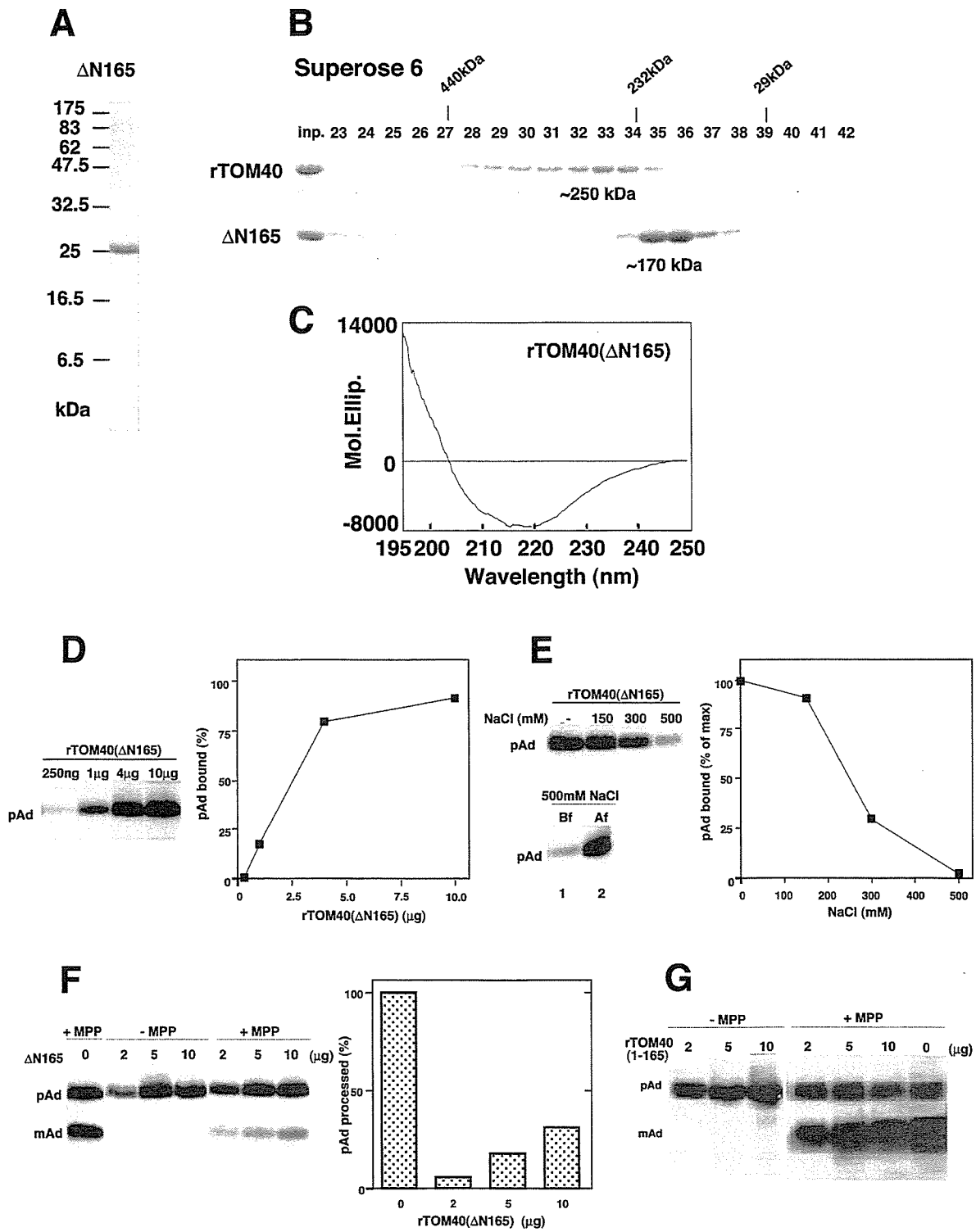

FIG. 5. **Structural characteristics of purified rTOM40(ΔN165) and its properties of preprotein recognition.** *A*, SDS-PAGE profile of purified rTOM40(ΔN165). *B*, elution profiles of rTOM40 and rTOM40(ΔN165) through Superose 6 column equilibrated with 20 mM Tris-HCl (pH 7.5) containing 0.5% Brij35 and 150 mM NaCl. *C*, CD spectrum of rTOM40(ΔN165). *D*, binding of pAd by rTOM40(ΔN165) as assessed by pull-down assay. pAd (1 μg) was incubated with the indicated amounts of rTOM40(ΔN165) (N-terminal His_6-tagged), and then the reaction mixtures were subjected to pull-down reaction. Other conditions were as described in the legend to Fig. 3. *E*, salt sensitivity of the pAd·rTOM40(ΔN165) complex. The binding assay was performed as in *D* using 5 μg of rTOM40(ΔN165) in the presence of the indicated concentrations of NaCl. *F*, sequestration of the MPP-processing site of pAd within rTOM40(ΔN165) molecule. pAd and rTOM40(ΔN165) were incubated at 30 °C for 30 min. The reaction mixtures were then incubated with Ni-NTA beads. The pAd·rTOM40(ΔN165) complex was incubated with (+) or without (−) MPP at 30 °C for 30 min, and the reaction mixtures were analyzed by SDS-PAGE and subsequent immunoblotting with anti-adrenodoxin antibodies. In a separate experiment (ΔN165 = 0 μg), pAd was incubated with MPP at 30 °C for 30 min, and the reaction mixture was analyzed by SDS-PAGE and subsequent immunoblotting. The band intensities were quantified, and the processing efficiency (mAd/(pAd + mAd)) was calculated by setting the efficiency in the absence of rTOM40(ΔN165) to 100% (shown in the *right panel*). *G*, rTOM40-(1–165) binds pAd but does not sequester the MPP-processing site within the molecule. The indicated amounts of N-terminal His_6-tagged rTOM40-(1–165) were incubated in 200 μl with 1 μg of pAd, and the reaction mixtures were subjected to the MPP protection assay as described in *F*.

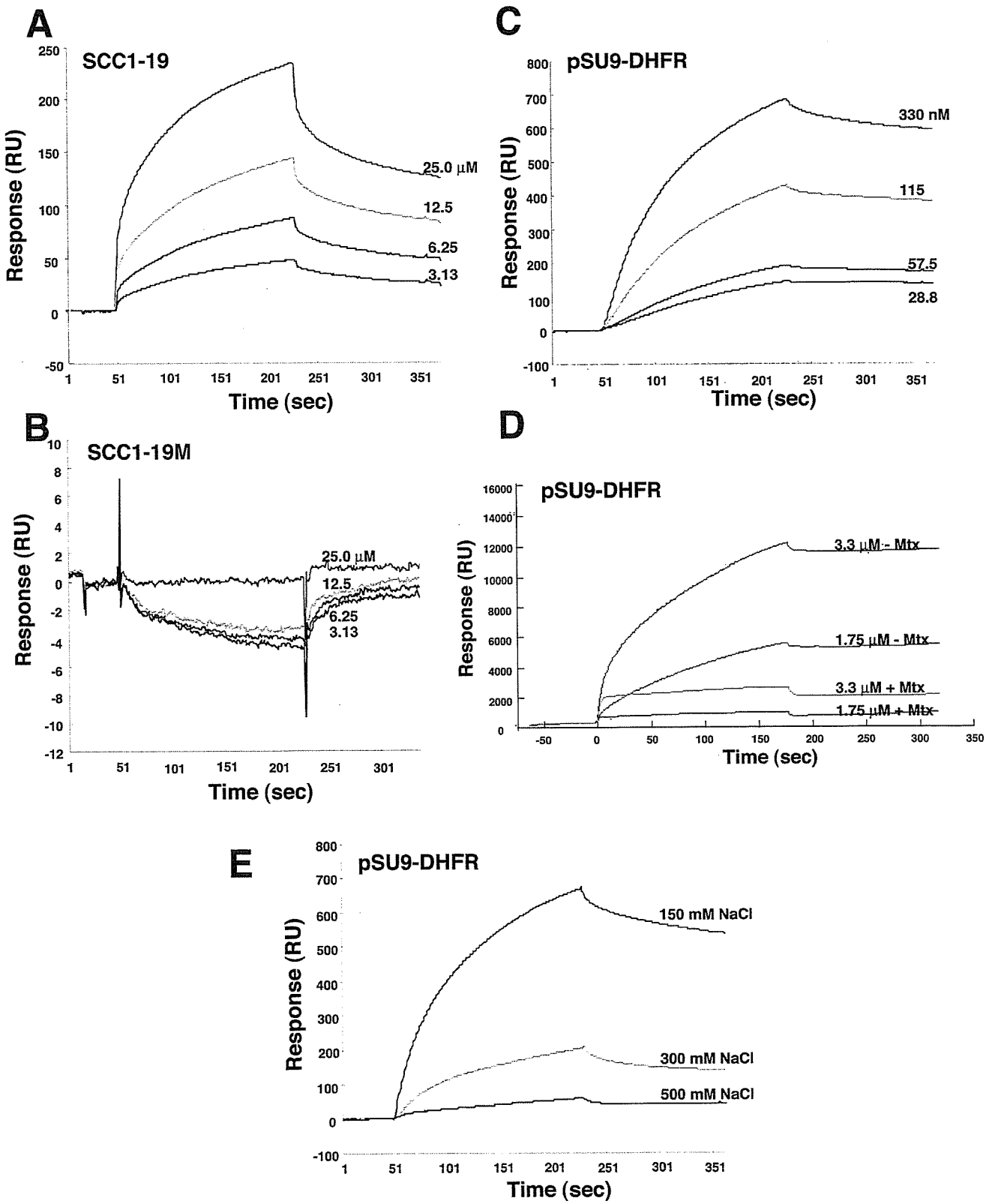

FIG. 6. **Interaction of the presequence peptide or pSU9-DHFR with rTOM40 as assessed by SPR.** *A*, SCC1–19; *B*, SCC1–19M; or *C*, pSU9-DHFR in running buffer containing 0.05% Brij35 was injected to rTOM40-immobilized sensor chip at 25 °C. *D*, pSU9-DHFR pretreated with or without methotrexate (*Mtx*) at 0 °C for 30 min was injected into the sensor chip. Other conditions were described under "Experimental Procedures." *E*, interaction of rTOM40 and pSU9-DHFR was performed in running buffer containing the indicated concentrations of NaCl.

40–1, and 189–207: peptide 40–2) recognized all three fragments (Fig. 4*B*). On the other hand, anti-His_6 antibodies only recognized the full-size rTOM40 (Fig. 4*B*). Thus, rTOM40 antibodies recognized the epitopes located within the N-terminal 65 residues of rTOM40. These results indicated that the C-terminal half of rTOM40 (residues 166–361; 21.4 kDa) folded

to form a stable domain structure.

We then addressed the topology of rTOM40 in the mitochondrial outer membrane using antibodies against rTOM40 (α-TOM40) and against a synthetic peptide corresponding to residues 189–207 (α-peptide 40-2). Elastase treatment of rat liver mitochondria under isotonic conditions produced a fragment, which was recognized both by α-TOM40 and α-peptide 40-2(Fig. 4*C*, *left* and *middle panels*). Under hypotonic conditions, elastase produced a fragment, which was detected only by α-peptide 40-2 (Fig, 4*C*, *middle panel*). From the size and reactivity with the antibodies, the bands produced under isotonic conditions and hypotonic conditions were considered to correspond to fragment 1 and fragment 2, respectively. These results indicated that the N-terminal site (Ala^7–Ser^8) of rTOM40 is exposed to the outer surface of the mitochondria, whereas the site Ala^{65}–Ala^{66} is localized in the intermembrane space. The Ile^{165}–His^{166} site, which is accessible to elastase in purified rTOM40 to produce fragment 3, was masked by the membrane or by the components of the TOM complex. The behavior of mitochondrial markers, mHsp70 (matrix protein), TIM23 (inner membrane protein extruding the N-terminal segment out of the inner membrane), and TOM20 (outer membrane protein extruding the bulk C-terminal portion to the cytosol), indicated that the protease digestion reactions were well controlled (Fig. 4*C*, *right panel*). Of note, fragments 1 and 2 were resistant to sodium carbonate (pH 11.5) extraction, indicating that they were firmly embedded in the membrane (data not shown). Topology of the N-terminal segment was further confirmed by using mitochondria isolated from HeLa cells expressing N-terminal His_6-tagged rTOM40. As shown in Fig. 4*D*, the His_6 epitope tag was removed by elastase treatment under isotonic conditions, indicating that the N-terminal segment of rTOM40 is exposed to the cytosol. We then probed the orientation of the C-terminal segment by using mitochondria harboring C-terminal hemagglutinin (HA)-tagged rTOM40. When the mitochondria were treated with proteinase K under isotonic conditions, the HA tag was unaffected, whereas it was completely removed from rTOM40 when the outer membrane was ruptured by hypotonic treatment, thus indicating that the C-terminal segment is exposed to the intermembrane space (Fig. 4*D*, *right panel*). This was further confirmed by carboxypeptidase Y treatment. rTOM40 in the isolated mitochondria was resistant to carboxypeptidase Y treatment under isotonic conditions, whereas it was completely digested under hypotonic conditions or in the presence of Triton X-100 (Fig. 4*E*). As a control, rTOM22 that is inserted into the outer membrane in the N_{out}-C_{in} orientation exhibited the same susceptibility to the carboxypeptidase Y treatment (Fig. 4*E*). Taken together, rTOM40 is embedded in the outer membrane exposing its N-terminal segment to the cytosol and the C-terminal segment to the intermembrane space, whereas at least the site Ala^{65}–Ala^{66} is exposed to the intermembrane space (Fig. 4*F*). Whether segment 1–165 is embedded in the membrane by a single or multispanning configuration remains to be determined. The predicted overall topology is distinct from that of *N. crassa* Tom40; the N- and C-terminal ends are exposed to the intermembrane space (28, 29). The N-terminal segment of *S. cerevisiae* Tom40 is exposed to the cytosol (12), but the topology of the C-terminal segment is not known.

rTOM40(ΔN165) Has a Secondary Structure and Preprotein-binding Properties Comparable with rTOM40—Based on the above findings, we purified a recombinant protein rTOM40(ΔN165) (21.4 kDa) in which the N-terminal 165-residue segment of rTOM40 was deleted, essentially according to the procedure adopted for rTOM40 (Fig. 5*A*). On a Superose 6 gel filtration column, it was eluted at an apparent molecular size of ~170 kDa with a sharp elution peak compared with rTOM40 (Fig. 5*B*). The secondary structure calculated from the CD spectrum in 0.5% Brij35 (Fig. 5*C*) revealed 62.0% β-sheet, 1.8% α-helix, 1.8% turn, and 34.5% random structures.

TABLE I
WT indicate wild type Kinetic parameters by surface plasmon resonance

TOM40		SCC 1–19	pSU9-DHFR
WT (full)	k_a (M^{-1} s^{-1})	3.0×10^2	3.1×10^4
	k_d (s^{-1})	8.7×10^{-4}	3.7×10^{-6}
	K_D (k_d/k_a)	3.0×10^{-6}	1.2×10^{-10}
ΔN165	k_a (M^{-1} s^{-1})	1.8×10^2	2.9×10^4
	k_d (s^{-1})	8.7×10^{-4}	2.3×10^{-5}
	K_D (k_d/k_a)	4.9×10^{-6}	8.0×10^{-10}

rTOM40(ΔN165) had preprotein-binding properties comparable with those of rTOM40 as follows: (i) dose-dependent pAd binding (Fig. 5*D*); (ii) salt-sensitive initial binding of pAd, followed by salt-resistant binding (Fig. 5*E*); and (iii) sequestration of the MPP processing site within the rTOM40(ΔN165) pore (Fig. 5*F*). It should be noted that the purified recombinant form of segment 1–165 of rTOM40 (rTOM40-(1–165)) bound pSU9-DHFR with a K_D of 1.4×10^{-10} M as assessed by SPR measurements (data not shown), but it failed to protect the precursor from attack by MPP (Fig. 5*G*), suggesting that the protection against MPP was because of specific interactions with rTOM40(ΔN165). Taken together, rTOM40(ΔN165) exhibited preprotein recognition properties as the import pore comparable with those of rTOM40. In support of these findings, rTOM40 and rTOM40(ΔN165) reconstituted into proteoliposomes exhibited permease activity for the vesicle-entrapped sucrose (see below).

Binding Kinetics of Preproteins to rTOM40 and rTOM40-(ΔN165) as Analyzed by SPR—We next measured the kinetics of interaction of rTOM40 or rTOM40(ΔN165) with either the synthetic presequence SCC1–19 or recombinant pSU9-DHFR by using SPR. rTOM40 or rTOM40(ΔN165) was immobilized to the sensor tips, and various concentrations of presequence or pSU9-DHFR were injected. The binding curves obtained (Fig. 6 for rTOM40; data not shown for rTOM40(ΔN165)) were analyzed by using BIA Evaluation software. Calculated association (k_a) and dissociation (k_d) rate constants and K_D (k_d/k_a) values are summarized in Table I. The affinity of rTOM40 for presequence peptide SCC1–19 was 3.0×10^{-6} M (Table I). No binding was observed with nonfunctional control peptides SCC1–19M (20) (Fig. 6*B*) and Synb2 (30) (data not shown). In contrast, however, rTOM40 exhibited ~10^4-fold higher affinity (1.2×10^{-10} M) for pSU9-DHFR compared with the synthetic presequence, suggesting that the mature segment of the precursor was responsible for the high affinity binding (Fig. 6*C* and Table I). When the conformation of the DHFR segment was stabilized with methotrexate, binding of pSU9-DHFR was strongly inhibited (Fig. 6*D*). Taken together, these results suggested that the affinity of rTOM40 for the presequence *per se* was rather low, and the affinity was greatly increased by the presence of the unfolded mature region of the preprotein.

We then examined the salt sensitivity of the interaction between rTOM40 and pSU9-DHFR. The interaction was salt-sensitive, and the binding was almost completely inhibited by 0.5 M NaCl (Fig. 6*E*), confirming the results of the pull-down assays (see Fig. 3). These results indicated that rTOM40 initially binds preproteins mainly through ionic interactions, which is followed by some other interactions including hydrophobic forces; the unfolded mature segment of preprotein seemed to contribute to the latter interactions (13). rTOM40(ΔN165) exhibited similar but slightly lower affinity

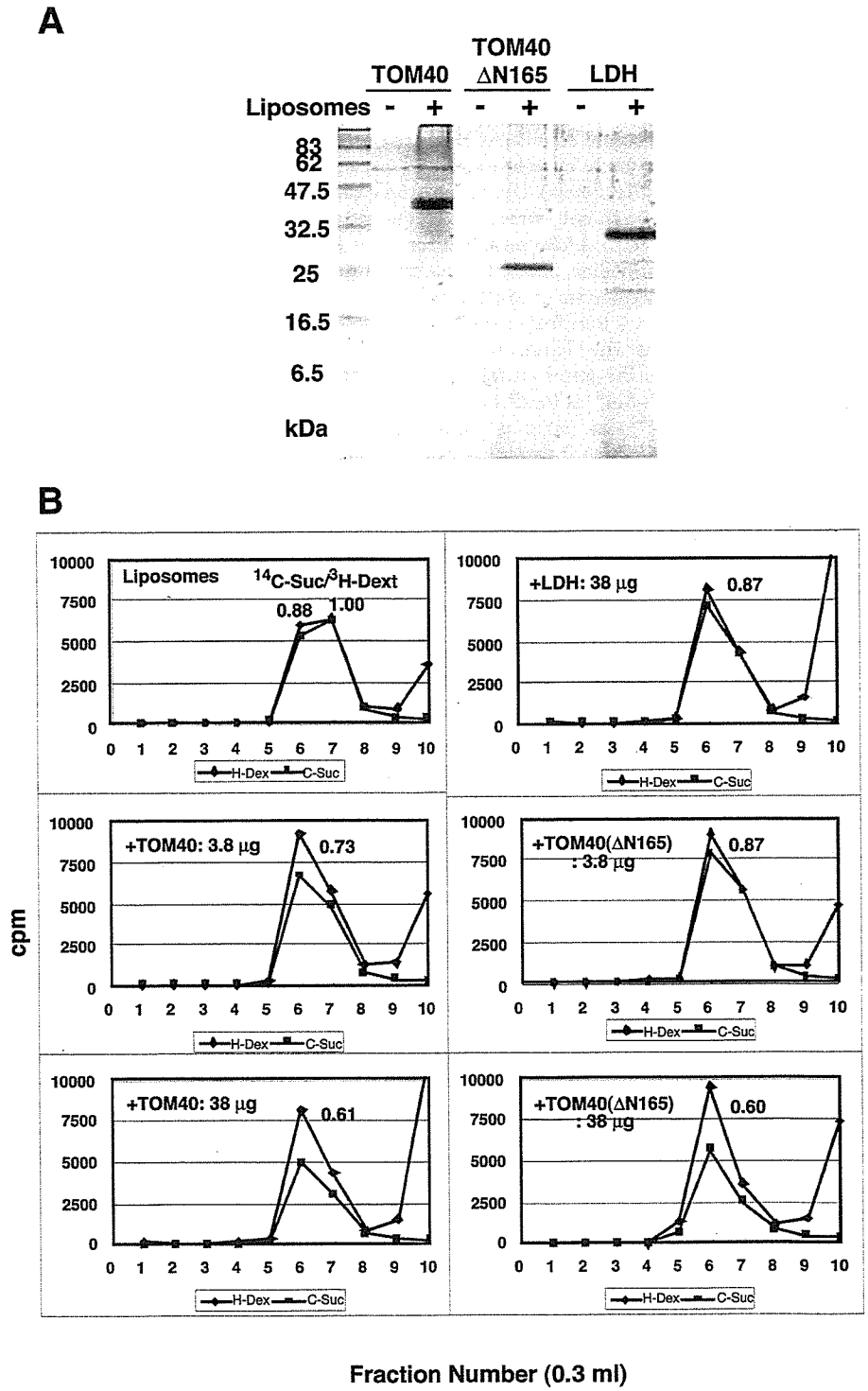

FIG. 7. **Sucrose passage activity of rTOM40 and rTOM40(ΔN165).** *A*, reconstituted proteoliposomes (asolectin +) or mock-treated proteins (asolectin −) were subjected to centrifugal floatation at 100,000 rpm for 90 min. The 0.25 and 1.25 M sucrose layers containing proteoliposomes were collected and analyzed by SDS-PAGE and Coomassie Brilliant Blue staining. As the control, mock-treated proteins remained in the bottom fractions of the tubes. *B*, elution profiles of the [^{14}C]sucrose- and [^{3}H]dextran-entrapped proteoliposomes. [^{14}C]Sucrose and [^{3}H]-dextran were enclosed in the proteoliposomes reconstituted with asolectin and the indicated proteins. The reaction mixtures were subjected to gel filtration through Sepharose CL-4B. Radioactivities of the eluted fractions were measured. The ^{14}C/^{3}H ratios of the peak fractions were normalized so that those of the incubation mixtures would be equal to 1.0. Other conditions were described under "Experimental Procedures." *LDH*, lactate dehydrogenase.

for SCC1–19 and pSU9-DHFR compared with full size rTOM40 (Table I and data not shown). The N-terminal 165 segment might contribute to stabilize the correct conformation of the pore-forming segment.

rTOM40 and rTOM40(ΔN165) Exhibit Sucrose Passage Activity When Reconstituted into Liposomes—Because our attempts to measure the channel activity for rTOM40(ΔN165) by using electrical methods were unsuccessful for technical reasons, we tried to measure the pore activity biochemically. Because the TOM complex, when reconstituted into proteoliposomes, mediates passage of small molecules (11, 31), we examined whether rTOM40(ΔN165) has sucrose passage activity, using the method adopted for measuring the activity of mitochondrial porin (17, 32). This assay measures the retention of large [^{3}H]dextran (mean M_r 70,000) *versus* small [^{14}C]sucrose that had been trapped into proteoliposomes containing rTOM40 proteins by sieving through a Sepharose 4B column. These experiments revealed that both rTOM40 and rTOM40(ΔN165) mediated passage of sucrose to a significant extent (Fig. 7 and Table II). As the controls, heat-denatured rTOM40(ΔN165) and cytoplasmic enzyme lactate dehydrogenase were inactive in this assay. We thus concluded that the